Microtubule occupancy at kinetochores links checkpoint silencing with mitotic memory

Joana Soares-de-Oliveira[1,2,3#], Naoyuki Okada[1,2,#], Tobias Kletter[1,2,#], Elias S. Weiler[1,2,3], António J. Pereira[1,2], Helder Maiato[1,2,4,*]

[1] Chromosome Instability & Dynamics Group, i3S - Instituto de Investigação e Inovação em Saúde, Universidade do Porto, Rua Alfredo Allen 208, 4200-135 Porto, Portugal

[2] Instituto de Biologia Molecular e Celular, Universidade do Porto, Rua Alfredo Allen 208, 4200-135 Porto, Portugal

[3] ICBAS-Instituto de Ciências Biomédicas Abel Salazar, University of Porto, Rua Jorge de Ferreira 228, 4050-313 Porto

[4] Cell Division Group, Department of Biomedicine, Faculdade de Medicina, Universidade do Porto, Alameda Prof. Hernâni Monteiro, 4200-319 Porto, Portugal

[#] Equal contribution

* Correspondence to: maiato@i3s.up.pt

Abstract

The spindle assembly checkpoint (SAC) promotes faithful chromosome segregation by delaying mitosis until all kinetochores attach to spindle microtubules. Paradoxically, a p53-dependent memory mechanism - the “mitotic stopwatch” - blocks daughter cell proliferation after unusually prolonged mitoses. Understanding how the SAC coordinates with the mitotic stopwatch is critical to disentangle this conundrum. Here, we found that microtubule occupancy at kinetochores is a cornerstone linking SAC silencing with mitotic memory. By combining live-cell with super-resolution microscopy, FRAP, laser microsurgery and molecular perturbations in Indian muntjac fibroblasts, we show that SAC silencing at kinetochores is gradual, non-uniform and confined to highly-localized microtubule attachments. Augmin promotes timely SAC silencing with maximal microtubule occupancy at kinetochores, whereas MPS1/CDK1 inhibition bypasses this condition. Partial microtubule occupancy delays SAC silencing, increases segregation errors and blocks daughter cell proliferation. Thus, timely SAC silencing with high microtubule occupancy avoids “bad memories” of mitosis to allow daughter cell proliferation.

Introduction

Faithful chromosome segregation during mitosis is essential for tissue homeostasis. Errors in chromosome segregation may lead to aneuploidy compromising cell viability, or drive chromosomal instability, a hallmark of human cancers implicated in tumor evolution, metastasis, therapy resistance, and reduced patient survival [1]. To promote faithful chromosome segregation during mitosis, the spindle assembly checkpoint (SAC) delays anaphase until all kinetochores attach to mitotic spindle microtubules [2]. At the root of the SAC signaling cascade, a MAD1/MAD2 complex recruited to unattached kinetochores initiates a catalytic process that activates free cytosolic MAD2 to bind CDC20, BUBR1 and BUB3, producing a diffusible Mitotic Checkpoint Complex (MCC). The MCC inhibits the Anaphase Promoting Complex/Cyclosome (APC/C), an E3-ubiquitin ligase that otherwise targets Cyclin B1 and Securin for degradation by the proteasome (reviewed in [3-5]). This releases the cysteine-protease Separase to cleave the Cohesin molecules that hold sister-chromatids together, thereby triggering their initial separation in anaphase, while preventing SAC reactivation during anaphase [6,7].

Upon kinetochore attachment to microtubules, SAC strength gradually decreases as result of the removal of MAD1/MAD2, eventually halting the catalytic cascade underlying MCC production [8,9]. The removal of MAD1/MAD2 from kinetochores during SAC silencing is mediated by PP1 and PP2A phosphatases, which are recruited by the outer kinetochore component KNL1 to oppose the action of key mitotic kinases, such as CDK1 and MPS1[10-15]. As microtubules establish end-on attachments, MPS1 is outcompeted from NDC80 complexes at kinetochores[16,17], and the MAD1/MAD2 complex is removed by dynein-mediated stripping as the fibrous corona disassembles[18-22].

Pioneering correlative light and electron microscopy work in PtK1 cells showed that their kinetochores bind more microtubules in anaphase than in metaphase, indicating that SAC silencing during normal mitosis can occur at ~85% microtubule occupancy at kinetochores [23]. Classic micromanipulation experiments in grasshopper spermatocytes further indicated that weakly attached kinetochores with less than 40% microtubule occupancy show greatly

diminished MAD1/MAD2 recruitment when compared with fully unattached kinetochores, delaying but not preventing anaphase onset [24]. Indeed, in this system, high microtubule occupancy was found to be necessary for the reliable and complete removal of MAD1/MAD2 from kinetochores [24]. In contrast, two recent studies in human HeLa cells overexpressing individual or combinations of Hec1 phosphomimetic mutants to create intermediate average microtubule attachment states at kinetochores estimated that 20–50% of the normal metaphase microtubule occupancy is sufficient to trigger complete and uniform removal of MAD1/MAD2 from kinetochores [25,26]. However, this switch-like model remains difficult to reconcile with the finding that the rate of MAD1/MAD2 loss from kinetochores increases with microtubule occupancy, with SAC silencing under conditions of low microtubule occupancy resulting in extensive mitotic delays [24-26]. A third study in human RPE1 cells used a microtubule depolymerizing drug to reduce microtubule occupancy at kinetochores [27]. Based on direct microtubule counting by electron microscopy, this study showed that ~70% microtubule occupancy at metaphase kinetochores is sufficient to silence the SAC, with less than 5 min delay relative to controls, but at the price of increasing the incidence of lagging chromosomes during anaphase [27]. Thus, although cells can silence the SAC with low microtubule occupancy, there may be selective pressure for high microtubule occupancy at kinetochores before initiating anaphase, ensuring proper chromosome segregation and avoiding significant mitotic delays [27,28]. This hypothesis gains weight in light of the recently uncovered “mitotic stopwatch” complex formed by 53BP1 and the deubiquitinase USP28 that stabilizes p53 in response to even moderate delays in mitosis, leading to subsequent cell cycle arrest or death in G1, independently of DNA damage [29-36]. However, how SAC silencing is coordinated with the mitotic stopwatch to control daughter cell proliferation remains unknown.

Here we set to investigate whether and how the SAC responds to highly-localized microtubule attachments at kinetochores, while testing whether the extent of microtubule occupancy underlying SAC silencing impacts daughter cell proliferation. Overall, our data support a gradual, non-uniform (i.e. confined to highly-localized microtubule attachments), SAC-silencing mechanism that is

assisted by Augmin to promote high microtubule occupancy at kinetochores for timely and faithful chromosome segregation. Importantly, if cells ultimately silence the SAC after experiencing significant mitotic delays due to low microtubule occupancy at kinetochores, the resulting daughter cells are bookmarked to prevent their proliferation and the potential propagation of segregation errors.

Results

MAD1 is gradually removed from Indian muntjac kinetochores in a microtubule-dependent manner

According to the switch-like SAC-silencing model, kinetochores respond as a single unit to silence the SAC after just a few microtubule attachments are established [25,26]. However, because human kinetochores cannot be resolved by conventional light microscopy, this postulate has so far been impossible to test experimentally. To overcome this limitation, we took advantage of the unique cytological features of female Indian muntjac fibroblasts, which carry only six chromosomes with naturally "super-resolved" kinetochores that arose by tandem and centric fusions of smaller ancestral chromosomes [37-43]. As a first step towards investigating SAC silencing in this system, we determined the time between MAD1 disappearance from kinetochores and anaphase onset by tracking individual kinetochores in live, hTERT-immortalized, female Indian muntjac fibroblasts stably expressing mScarlet-CENP-A (a constitutive kinetochore marker) and Venus-MAD1 [8]. We found that MAD1 signal at kinetochores became essentially undetectable ~20 min before anaphase onset (Fig. S1A, B), in agreement with previous reports in other vertebrate cell lines [44,45] and consistent with the temporal framework of anaphase onset upon laser-mediated ablation of the last unattached kinetochore [2].

To determine the kinetics of SAC silencing in response to microtubule attachments at individual kinetochores in live Indian muntjac fibroblasts, we combined stable expression of fluorescent Venus-MAD1 with carefully titrated SiR-tubulin [41] under slight cell compression to improve visualization [42]. As a control, cytoplasmic Venus-MAD1 signal was simultaneously measured, and photobleaching was found to be negligible throughout the course of the experiment (Fig. S1C). MAD1 decayed gradually at individual kinetochores as chromosomes bi-oriented and aligned at the equator during prometaphase (Figure 1A, C), with a rate of decay that was well fit to a single exponential (Figure 1E and Fig.S2), in agreement with previous reports in Ptk2 cells [46]. Noteworthy, pole-proximal chromosomes aligned last and did so tangentially along the

curvature of the spindle edge. Moreover, their leading kinetochores were enriched with MAD1 from the onset of congression, with the signal gradually decreasing as chromosomes approached the equator (Figure 1A, A', A''). Importantly, MAD1 typically decayed first on trailing kinetochores, likely reflecting differences in the timing or efficiency in the formation of stable end-on microtubule attachments compared with leading kinetochores. (Figure 1A, A', A''). These results are fully consistent with congression models where pole-proximal, mono-oriented chromosomes use plus-end-directed motors on the leading kinetochore to initiate lateral gliding along pre-existing spindle microtubules towards the equator [46-49], while at odds with models where stabilization of end-on attachments and bi-orientation take place before pole-proximal chromosomes initiate congression [50].

To test whether gradual MAD1 decay at kinetochores during mitosis depends on microtubule occupancy, we monitored MAD1 levels in the presence of 1 µM nocodazole, which depolymerized all spindle microtubules. As expected, under these conditions, MAD1 localized on every kinetochore for over 20 min, without any measurable decay (Figure 1B, C and Fig. S2). These data indicate that gradual SAC silencing during mitosis depends on the establishment of microtubule attachments at kinetochores.

MAD1 is rapidly removed from Indian muntjac kinetochores upon MPS1 or CDK1 inactivation, regardless of microtubule occupancy

MPS1 and CDK1 kinases are critical to maintain SAC signaling by counteracting the activities of PP1 and PP2A phosphatases required for mitotic exit [10-15]. Therefore, we next investigated the kinetics of MAD1 decay at kinetochores after acute MPS1 or CDK1 inactivation with MPS1-IN-1 [51] or RO 3306 [52], respectively. We found that MAD1 decayed more abruptly from kinetochores after MPS1 or CDK1 inhibition, regardless of microtubule occupancy, reaching 50% of the initial levels 3.8x or 1.5x faster than during normal mitosis, respectively (Figure 1B, C, E and Fig. S2). These data indicate that inactivation of MPS1 or CDK1 can bypass the requirement of a given microtubule occupancy at kinetochores to silence the SAC.

MAD1 removal depends on kinetochore size

A prediction from switch-like models that favor independent microtubule binding at kinetochores and where a given percentage of occupancy is key to uniformly silence the SAC [25,26] is that small or large kinetochores would simultaneously reach the same percentage of occupancy (and, consequently, have similar MAD1 half reduction times), despite binding a different total number of microtubules. However, despite ample evidence of kinetochore size differences in humans [53-61], this prediction is currently impossible to test experimentally in human cells for the same reasons evoked before. In contrast, the large kinetochore from chromosome 3+X in female Indian muntjac cells can be unequivocally distinguished from those on the smaller chromosomes 1 and 2, allowing us to track MAD1 decay as a function of kinetochore size [38,40,41]. Surprisingly, we found that MAD1 signal on the large kinetochores of chromosome 3+X requires ~38% more time to become undetectable, when compared with smaller kinetochores on chromosomes 1 and 2 (Figure 1D, E, and Fig. S2). These findings suggest that switch-like models do not fully account for how the SAC is normally silenced.

MAD1 is immobile within kinetochores

In order to obtain a deeper understanding of the mechanisms underlying SAC silencing we investigated MAD1 dynamics within kinetochores. Two possible scenarios could be envisioned: 1) if MAD1 is mobile within kinetochores, few microtubule attachments might be sufficient to “extinguish” all MAD1, for example by Dynein-mediated stripping along microtubules [18,19] (Figure 2A); 2) if MAD1 is immobile within kinetochores, Dynein-mediated stripping along microtubules would be confined to the sites or domains where microtubules are attached (Figure 2A). To distinguish between these two scenarios, we photobleached Venus-MAD1 on a fraction (up to 50%) of the large kinetochore from chromosome 3+X in the absence of microtubules. Clear predictions about MAD1 mobility within kinetochores could be made, depending on the FRAP profile. If MAD1 is mobile within kinetochores, the photobleached fraction of the kinetochore is expected to recover due to migration of fluorescent Venus-MAD1 molecules from the unbleached fraction, resulting in the convergence of signals

to an intermediate and uniform level along the entire kinetochore (Figure 2A'). In contrast, if MAD1 is immobile within kinetochores, the photobleached fraction of the kinetochore would be expected to only recover fluorescent Venus-MAD1 molecules that are exchanging with the cytoplasmic pool, while the unbleached fraction would remain stable over time (Figure 2A'). We were successful in partially photobleaching Venus-MAD1 in a fraction of the kinetochore, with minimal/unintended photobleaching of Venus-MAD1 on the remaining fraction (Figure 2B-B''). Importantly, after photobleaching of the intended fraction of the kinetochore, Venus-MAD1 fluorescence recovered up to ~50%, with a half recovery time of 2-6 seconds, while remaining stable (or increasing slightly; see ahead) over time in the unbleached fraction (Figure 2B-B'', D, E). As a control, we photobleached Venus-MAD1 on entire kinetochores, which resulted in identical recovery parameters when compared to partial photobleaching, and in line with previous measurements in other mammalian systems [44,45] (Figure 2C-C'', D, E). Because fluorescence recovery of the mobile fraction of Venus-MAD1 after photobleaching entire kinetochores is exclusively due to exchange with the cytoplasmic pool [44,45], we concluded that this pool also accounts for the observed fluorescence recovery of Venus-MAD1 on partially photobleached kinetochores. Taken together, these data indicate that MAD1 is essentially immobile within kinetochores, suggesting that it can only be removed from spatially confined regions upon the establishment of highly-localized microtubule attachments or by a microtubule-independent SAC-silencing mechanism, such as the one involving CDK1 or MPS1 inactivation.

MAD1 removal along individual kinetochores is non-uniform and confined to highly-localized microtubule attachments

The conclusion from our FRAP experiments implies that, in a normal mitosis, there may be low microtubule occupancy states in which MAD1 removal is limited to regions where microtubule attachments are established. To test this prediction, we monitored Venus-MAD1 decay along the entire kinetochore length as microtubules attach during mitosis. Near-simultaneous tracking of individual kinetochores, MAD1 and microtubules in living cells revealed a non-uniform

decay of MAD1 along kinetochores (Figure 3A, B). To further dissect the relationship between non-uniform MAD1 decay and microtubule occupancy along kinetochores, we used super-resolution CH-STED microscopy [62] and 3D image rendering to inspect (fixed) late prometaphase cells with only partial MAD1 signal along kinetochores (Figure 4A, B and Fig. S3A, B). We found clear examples where fractions of the kinetochore had end-on attached microtubules with no detectable MAD1, while other fractions were devoid of microtubules and clearly enriched for MAD1 (Figure 4A, B and Fig. S3A, B). A line scanning profile along the entire length of several such individual kinetochores confirmed a negative correlation between MAD1 signal and microtubule density in 15/21 (71.4%) of the cases (Figure 4C, D and Fig. S3A', B').

To improve the resolution of our analyses we divided the longitudinal axis of partially attached kinetochores into multiple subsections and quantified MAD1 and microtubule intensity at each subsection (Figure 4E). We found a weak, yet highly significant, negative correlation between MAD1 and microtubule signal intensity along kinetochores (Figure 4F and Fig. S3C). Of note, the resulting L-shape curve indicates that while high microtubule signal is a good predictor of the absence of MAD1 at kinetochores, the opposite is not the case, suggesting that there are regions at kinetochores without microtubules that have no detectable MAD1, consistent with models evoking cooperative microtubule binding at kinetochores [63,64]. Overall, these data show that SAC silencing at kinetochores is non-uniform and confined to highly-localized microtubule attachments.

Local perturbation of kinetochore function results in a local SAC response to microtubule attachments/detachments

To directly test how the SAC responds to localized microtubule attachments/detachments, we used laser microsurgery to partially ablate individual metaphase kinetochores (and, consequently, microtubules that were attached to the ablated region) upon SAC silencing in live Indian muntjac fibroblasts (Figure 5A). These cells stably expressed GFP-CENTRIN-1 to mark spindle pole positions, 2xGFP-CENP-A to define the kinetochore target, and

mScarlet-MAD1 to monitor SAC status before and after surgery (Figure 5B). We found that, within few minutes after partial kinetochore ablation, the unperturbed sister kinetochore typically bent towards the attached spindle pole without any detectable MAD1 (Figure 5A-C). However, ~5 min after bending, MAD1 was often recruited to the tip of the bent unperturbed sister kinetochore, presumably due to highly-localized microtubule detachments (Figure 5A-D). In other cases, MAD1 was recruited to a more central region of the bent unperturbed sister kinetochore (Fig. S4A, A', B). Strikingly, in all cases MAD1 accumulation was highly localized and distinct from the uniform accumulation of MAD1 on fully unattached kinetochores resulting from nocodazole treatment (Figure 5B, D, E). Therefore, local kinetochore perturbations result in a highly-localized SAC response.

To assist us in the interpretation of the laser microsurgery data and determine whether the SAC was responding to microtubule detachments in the bent unperturbed sister kinetochore, we performed correlative super-resolution CH-STED microscopy after fixation of cells that showed MAD1 recruitment upon partial sister kinetochore laser ablation by live imaging (Figure 5F, F' and Fig. S4C, C'). We found that MAD1 accumulation, either at the tip or at a more central region of the unperturbed sister kinetochore, negatively correlated with microtubule density (Figure 5F', F'' and Fig. S4C', C''). We reasoned that MAD1 accumulation near the tip of the unperturbed kinetochore may result from highly localized microtubule detachments due to lack of tension in the partially ablated sister. In other cases, localized forces applied to both ends of the unperturbed kinetochore may generate enough tension along its length to allow a few microtubules to remain stably attached near the tip, resulting in more central accumulation of MAD1. These results demonstrate that the SAC responds locally to highly localized microtubule attachment/detachment events along kinetochores.

Low microtubule occupancy at kinetochores after Augmin depletion delays MAD1 removal and SAC silencing

Next, we sought to investigate the cellular consequences of low microtubule occupancy at kinetochores. To do so we monitored SAC silencing after RNAi-mediated depletion of HAUS6, a subunit of the Augmin complex required for K-fiber maturation [43,65]. We found that MAD1 decay from kinetochores was slowed-down in HAUS6-depleted cells, as revealed by ~50% increase in the half reduction time of MAD1 signal at kinetochores relative to mock-depleted controls (Figure 6A-C, Figure S2). Moreover, even when HAUS6-depleted cells were treated with the proteasome inhibitor MG132 for 1h to provide more time for K-fiber maturation, many more (66% vs. 12%) cells had at least one MAD1-positive kinetochore and overall higher MAD1 levels at kinetochores when compared with control metaphase cells (but lower than prometaphase levels) (Figure 6D, E). Closer inspection of mock- and HAUS6-depleted fixed cells with CH-STED super-resolution microscopy revealed that, while kinetochores in control mock-depleted metaphase cells treated with MG132 were abundantly occupied with microtubules and without detectable MAD1 signal, in HAUS6-depleted cells treated with MG132 MAD1 signal could still be detected along the kinetochores, despite interspersed end-on microtubule attachments (Figure 6F). However, unlike in control cells with clear partially attached kinetochores that showed a negative correlation between MAD1 and microtubule signal ($r = -0.29$, $p<1e-10$; Figure S5E), in HAUS6-depleted cells this correlation was lost ($r = -0.06$, $p=0.14$; Figure S5D, E and Figure S6C), suggesting that the resulting perturbations of microtubule occupancy were beyond our resolution capacity (Fig. S5A-C and Fig. S6A-B'). Overall, these data are in line with previous findings in human cells [25,26] indicating that low microtubule occupancy at kinetochores delays MAD1 removal from kinetochores and consequently SAC silencing.

Low microtubule occupancy delays SAC silencing, increases segregation errors, and blocks daughter cell proliferation

To further characterize the cellular consequences of low microtubule occupancy at kinetochores, we tracked HAUS6-depleted cells over several days by live-cell microscopy and determined their fates (Figure 7A). Mitoses in HAUS6-depleted

cells were significantly delayed and error-prone, proportional to the extent of HAUS6 depletion over time (Figure 7A' and B). When inspecting the outcomes resulting from mitotic delays in HAUS6-depleted cells more closely, we found three regimens. The majority of cells with mitotic durations below 200 minutes divided without segregation errors or spindle defects (Figure 7C). However, after a delay of approx. 200 minutes, virtually all cells divided with mitotic defects (Figure 7C), pointing towards persistently immature K-fibers at anaphase onset [27]. Strikingly, most cells that were stuck in mitosis for longer than 400 minutes eventually died in mitosis (Figure 7C).

To determine the fate of daughter cells from mothers that *did* divide despite immature K-fibers, we defined a cohort of cells that underwent mitosis within 12 and 36 hours of HAUS6 depletion and followed their offspring for 60 hours (Figure 7A). Strikingly, 74% of daughter cells arising from mitoses with durations longer than approx. 90 minutes stopped proliferating, whereas only 32% of daughter cells derived from shorter mitosis arrested (Figure 7D and S7F), in line with previous findings in human cells, suggesting active surveillance by the "mitotic stopwatch" [29,31,32,34]. To confirm that such a "memory" of mitotic duration is conserved in Indian muntjac cells, we tracked daughter cell fates after releasing cells from up to 6 hours of mitotic arrest mediated by the Eg5-inhibitor monastrol (Fig. S7A). In agreement with our observations in HAUS6-depleted cells, mother cells that experienced mitotic times longer than approx. 90 minutes gave rise to daughters that showed increased cell cycle lengths or stopped proliferating (>90 min mitosis - 61% of daughters arrested; <90 min mitosis - 30% of daughters arrested; Fig. S7B-F).

Together, these observations suggest the presence of a conserved mitotic stopwatch mechanism surveilling mitotic durations. Indeed, we were able to detect a significant accumulation of USP28 bound to 53BP1 – two components of the mitotic stopwatch complex – in Indian muntjac cells that experienced a prolonged mitosis (note that available anti-p53 monoclonal antibodies do not recognize the Indian muntjac protein under denatured conditions; Fig. S7G, H). However, since prolonged mitotic durations under low microtubule occupancy (i.e. HAUS6 depletion) or monastrol perturbation were tightly associated with

mitotic errors (Figures 7B, C and Fig. S7C, D) that may independently block daughter cell proliferation [66-69], we sought to disentangle the two events. To this end, the low chromosome number of Indian muntjac fibroblasts allowed us to unequivocally exclude cells dividing with errors from our cell fate analysis (Figure 7E and Fig. S7E, E', F). Remarkably, mother cells with increasing mitotic durations - but dividing error-free - were still increasingly more likely to give rise to daughter cells that arrest in G1 (Figure 7E and Fig. S7E, E', F), suggesting active "mitotic stopwatch" surveillance of mitotic duration.

Discussion

While there is a large consensus that SAC silencing can occur with low microtubule occupancy at kinetochores [23-27,46], whether and how SAC signaling along vertebrate kinetochores responds to highly localized microtubule attachments has remained a central open question. Current models suggest that mammalian kinetochores respond as a single unit that globally halts SAC signaling upon partial microtubule attachments [25,26,46]. As so, low microtubule occupancy would cause kinetochores to respond as a whole and predicts a uniform loss of MAD1 along the kinetochores. Moreover, these switch-like models imply the existence of a sensitive microtubule “counting” mechanism that determines SAC silencing when a given occupancy at each individual kinetochore is reached. However, in virtue of the sub-diffraction nature of most vertebrate (humans included) kinetochores, this prediction had never been directly tested and the essence of a putative microtubule “counting” mechanism remains elusive. In this regard, Indian muntjac kinetochores offer a unique setting to test these ideas. In stark contrast with the predictions from switch-like SAC-silencing models, we found that the removal of the SAC protein MAD1 from Indian muntjac kinetochores is gradual, non-uniform, correlates with local microtubule density and kinetochore size, and depends on Augmin-mediated maturation of K-fibers.

In line with previous work [46], MAD1 signal decay from Indian muntjac kinetochores was well fit by a single exponential, indicating that SAC silencing in this system faithfully replicates established kinetics in other vertebrate systems. Switch-like models that favor independent microtubule binding at kinetochores and where a given percentage of occupancy is key to uniformly silence the SAC [25,26], predict that the fraction of unattached sites is expected to decay exponentially, with a timescale that does not depend on kinetochore size. Interestingly, however, we found that MAD1 decay on large kinetochores was 38% slower compared to small kinetochores. While the underlying reasons for these differences remain unclear, this finding suggests that switch-like models do not fully account for how the SAC is normally silenced. Indeed, both live-cell imaging and super-resolution CH-STED analysis in Indian muntjac cells revealed

402 a non-uniform distribution of MAD1 on partially attached kinetochores that
403 negatively correlated with microtubule occupancy. Moreover, laser microsurgery
404 experiments demonstrated that once silenced, the SAC remains sensitive to
405 highly-localized microtubule detachments from kinetochores, even when more
406 than 50% occupancy persists. Lastly, experimental perturbation of microtubule
407 occupancy at kinetochores by interfering with K-fiber maturation significantly
408 delayed MAD1 removal and SAC silencing. Therefore, although low microtubule
409 occupancy at kinetochores may eventually silence the SAC, there is an
410 unavoidable impact on the respective mitotic duration. This has important
411 implications in light of the recently-uncovered "mitotic stopwatch" mechanism,
412 where even mild mitotic delays elicit a subsequent
413 USP28-53BP1-p53-dependent cell cycle arrest in G1 [29,31,32,35,70], and the
414 observation that SAC silencing with low microtubule occupancy increases the
415 incidence of lagging chromosomes during anaphase, potentially leading to
416 aneuploidy [27]. As so, the mechanism underlying SAC silencing at individual
417 kinetochores is likely to have evolved to maximize microtubule occupancy within
418 a strict temporal window to avoid "bad memories" of mitosis, and we show here
419 that the Augmin complex, through its role in K-fiber maturation [43,65], is
420 instrumental in this process (Figure 8).

421 But how do partially attached kinetochores that are locally sensitive to
422 microtubule attachments ultimately remove all MAD1/MAD2? In line with a model
423 in which the number of unattached kinetochores ultimately determines the rate of
424 MCC production that proportionally inhibits the APC/C [8,9], partially-attached
425 kinetochores may produce less MCC than fully unattached kinetochores [24].
426 Consequently, the APC/C would become sufficiently active and allow for slower,
427 yet steady, Cyclin B1 degradation (and CDK1 inactivation), ultimately silencing
428 the SAC after an extensive mitotic delay [24]. Whether kinetochores eventually
429 reach normal microtubule occupancy by the time the SAC is silenced after a
430 delay remains unclear (Figure 8), but it should be noted that even cells that are
431 unable to silence the SAC after extremely prolonged mitotic delays due to the
432 complete absence of microtubules degrade Cyclin B1 and eventually exit mitosis
433 due to residual APC/C activity [71,72]. Our finding that CDK1 inhibition triggers SAC

silencing irrespective of microtubule occupancy further supports this interpretation (Figure 8).

One may argue that the compound architecture of Indian muntjac kinetochores does not reflect what is normally found in other vertebrate species, including humans. However, we have no evidence that kinetochore architecture in Indian muntjac reflects a significant deviation at the level of the core microtubule-binding moduli, or other functional differences, including MAD1 decay during SAC silencing, when compared with other vertebrates [41,43,46,73]. Noteworthy, recent works have revealed that many human, mouse and chicken centromeres/kinetochores also have a compound, often bipartite, architecture [59,61,74,75]. In particular, the same human kinetochore could be found with one sub-domain end-on attached, and the other laterally attached to microtubules via the fibrous corona[74]. This is consistent with our finding of non-uniform, highly localized, MAD1 removal in response to local microtubule occupancy in Indian muntjac kinetochores. Importantly, while in these cases MAD1 and local microtubule density often negatively correlated along two apparently insulated adjacent domains on the same large kinetochore of chromosome 3+X (simply because these extreme cases are easier to detect), there were other cases (particularly evident after Augmin perturbation) where this negative correlation was observed along three or more sub-domains, without following a strict spatial pattern (also evident in the distinct responses after laser microsurgery experiments). Moreover, our finding that MAD1 is immobile within unattached kinetochores indicates that it can only be removed upon the establishment of highly-localized microtubule attachments (or eventually by a microtubule-independent SAC-silencing mechanism, such as MPS1 or CDK1 inactivation). Overall, our data favors a model where anaphase onset is determined by the gradual silencing of the SAC in response to highly localized microtubule attachments along the entire kinetochore length, rather than a uniform, switch-like mechanism. This model reconciles gradual SAC silencing with increasing microtubule occupancy at kinetochores, without the need for a dedicated microtubule “counting” system that triggers SAC inactivation. Most relevant, our finding that microtubule occupancy at kinetochores is at the root

between timely SAC silencing and mitotic memory, identifies a critical rate-limiting step with important implications for cell proliferation in mammals.

Materials and Methods

Cell lines and culture conditions

Indian muntjac cell lines were grown in Minimum Essential Media (MEM) (Corning), supplemented with 10% FBS (GIBCO, Life Technologies). Indian muntjac hTERT-immortalized fibroblasts were a gift from Jerry W. Shay [76]. IM fibroblasts stably expressing Venus-MAD1 were generated by lipofection of pVenus-MAD1 (kind gift from Jakob Nilsson [77]). RPE-1 hTERT-immortalized cells were cultured in DMEM (Corning™, 15323531) supplemented with 10% FBS (GIBCO, Life Technologies). All cells were kept at 37ºC in humidified conditions with 5% CO_2. Transfection was performed by incubating the cells with 1:400 Lipofectamine2000 (Invitrogen) in Opti-MEM (GIBCO, Life Technologies) for 6h, and stable and uniformly expressing cells were selected by FACS sorting (as detailed in [42]. For the production of Venus-MAD1 and mScarlet-CENP-A co-expressing cell line, Venus-MAD1 cells were transduced with pLVx-mScarlet-CENP-A lentiviral plasmid (generated in [43]). IM cells co-expressing 2x-GFP-CENP-A, GFP-CENTRIN-1 and mScarlet-MAD1 were produced by lentiviral transduction of pRRL-2x-EGFP-CENP-A (generated in [43]), pLVX-EGFP-C1-CENTRIN-1 (kind gift from Manuel Thery; Addgene plasmid # 73331) and pInducer-mScarlet-MAD1 (generated in this paper). Cells expressing GFP-H2B were produced by lentiviral transduction of LV-GFP (kind gift from Elaine Fuchs; Addgene plasmid # 25999). Lentiviral transduction was performed as detailed in [42]. Cells were incubated with lentivirus particles in the presence of 1:2000 Polybrene (Sigma-Aldrich; TR-1003) for 24h before supplied with fresh complete media. Stable lines with sufficient fluorescence intensity were selected by FACS sorting.

Plasmid design

pInducer-mScarlet-MAD1 was produced by cloning mScarlet (from pRRL-mScarlet-CENP-A) and MAD1 (from pVenus-MAD1) into the pInducer-20 backbone under a Tet-inducible promotor. To construct the empty backbone KASH-mCherry was removed by SalI + XhoI restriction digestion of pinducer 20

DN-KASH (kind gift from Daniel Conway; (Addgene plasmid # 125554)). Restriction sites were amplified from the plasmid by PCR (fwd: 5'-TTAAAGGAACCAATTCAGGCTAGCACGCGTATATCTAGACCCAGCTTTCT-3'; rev: 5'-TAAGCGTAGTCTGGGACG-3') and added to the emptied vector through Gibson assembly. mScarlet and MAD1 were cloned into the NheI linearized pInducer-20 backbone through Gibson assembly.

siRNA Experiments

Protein knockdown was performed as detailed in [42]. Briefly, IM fibroblasts seeded at 70% confluency were starved with MEM supplemented with 5% FBS for 30 minutes before transfection. siRNA transfection was performed by adding Lipofectamine RNAi Max (1:400; Invitrogen) and 50 nM of siRNA in serum free-medium (Opti-MEM, Gibco) for 6h before replacing the solution with fresh complete media. Cells were analyzed 72 hours after depletion. In long-term live cell imaging experiments (see below), siRNAs were not replaced with fresh medium and imaging started shortly after treatment. For the depletion of HAUS6, the following sequence was used: 5'-GGUUGGUCCUAAGUUUAUU[dT][dT]-3'[39]. Cells mock transfected (lipofectamine only) or transfected with luciferase-targeting siRNA were used as controls.

Drug Treatments

For acute inhibition of Mps1 and CDK1 kinases, 4 µM MPS1-IN-1 (kind gift from N.Gray [51]) and 10 µM RO 3306 (ChemCruz; CAS 872573-93-8), respectively, were added shortly after Nuclear Envelop Breakdown (NEB). To arrest cells in G2, these were treated with 10 µM RO 3306 for 14h. Microtubule depolymerization was triggered using 1 or 3.3 µM of Nocodazole (Sigma-Aldrich; CAS 31430-18-9) for 30 mins before the analysis. To increase mitotic duration cells were arrested in prometaphase with 100 µL of Monastrol (Tocris Bioscience, Cat. No.1305). Metaphase arrest was obtained using 5 µM MG132 (Sigma-Aldrich; CAS 133407-82-6). Fixed cell analysis using MG132 was

530 performed in the first 1.5 h after drug addition to avoid cohesion fatigue.
531 SiR-tubulin (Spirochrome; SC002) [78] was used to visualize microtubules, at 50
532 nM concentration incubated for 1 h prior to live-cell imaging. To induce p53
533 enrichment cells were treated with 5 µM etoposide (Selleck Chemicals, S1225) or
534 3.3 µM Nocodazole for 16h. The same volume of DMSO (Sigma-Aldrich, D4540)
535 was used as a control.
536
537 Immunofluorescence
538 Indian muntjac fibroblasts were seeded on fibronectin coated coverslips (#1.5
539 thickness) 24h before the experiment. Depending on the microscopy routine,
540 different fixation protocols were used: for widefield imaging cells were incubated
541 with 4% paraformaldehyde (Electron Microscopy Sciences) in PBS for 10 min at
542 room temperature; for STED microscopy PFA 4% supplemented with 0.1%-0.2 %
543 Glutaraldehyde (Electron Microscopy Sciences) in Cytoskeleten Buffer (CB -
544 274 mM NaCl, 10 mM KCl, 2.2 mM Na_2HPO_4, 0.8 mM KH_2PO_4, 4 mM EGTA,
545 4 mM $MgCl_2$, 10 mM Pipes, 10 mM glucose, pH 6.1) for 10 min at room
546 temperature was used; for same cell correlative live confocal and
547 super-resolution STED microscopy pre-warmed 2x concentrated PFA +
548 Glutaraldehyde diluted in imaging media to a final concentration of 4% and 0.2%,
549 respectively, was added to the imaging chamber. After a 5 min incubation at the
550 microscope (37ºC), the fixation solution was replaced with PFA 4%
551 supplemented with 0.2 % Glutaraldehyde in CB for an additional 5 min at room
552 temperature. Autofluorescence was quenched by a 0.1% sodium borohydride
553 solution (Sigma-Aldrich) for 7min. Cells were permeabilized with CB-0.5%Triton
554 for 20-30 min and blocked with CB-0.05% Tween 20 with 10% FBS (blocking
555 buffer) for 1 hour at RT. Samples were incubated with primary antibodies diluted
556 in blocking buffer over-night at 4ºC. The following primary antibodies were used:
557 human anti-centromere antiserum (ACA, Fitzgerald; 90C-CS1058) 1:2000/1:200
558 (Widefield/ STED); anti-tyrosinated tubulin (Bio-Rad; MCA77G) 1:2000/1:100
559 (Widefield/ STED); anti α-tubulin (clone B-5-1-2, Sigma-Aldrich; T5168) 1:100
560 (correlative live-cell and fixed STED microscopy). Cells were washed with
561 PBS-0.05% Tween before incubation with the corresponding secondary

antibodies for 1h at RT – Alexa Fluor 568 and 647 (Thermo Fisher Scientific) 1:1000; or abberior STAR 580 (Abberior Instruments; ST580) and abberior STAR-Red (Abberior Instruments; STRED) 1:200 for STED microscopy. DNA was labeled with a quick incubation in the presence of 1 µg/mL 4'6'-Diamidino-2-phenylindole (DAPI) in PBS-0.05% Tween. The samples were washed in PBS and mounted on glass slides with a mounting solution (20 mM Tris pH8, 0.5 N-propyl gallate, 90% glycerol).

Monitoring kinetochore MAD1 levels in live recordings

Indian muntjac fibroblasts stably expressing Venus-MAD1 or co-expressing Venus-MAD1 and mScarlet-CENP-A were plated on fibronectin coated glass bottom 35 mm FluoroDish (World Precision Instruments; FD35-100), 36-48h before imaging. Before imaging, normal culture media was replaced with Leibovitz's L15 medium (GIBCO, Life Technologies) supplemented with 10% FBS and the cell-permeable microtubule dye, SiR-tubulin. Live-cell imaging was performed on a temperature-controlled Nikon-Ti microscope equipped at the camera port with a Yokogawa CSU-X1 spinning-disc head with Borealis and an iXon+ DU-897 EM-CCD (Andor). Cells were imaged with an oil-immersion 60x 1.4 NA Plan-Apo DIC CFI objective (Nikon, lambda series), yielding a 176 nm/pixel sampling, or a 100x 1.4 NA Plan-Apo DIC CFI objective (Nikon, VC series), yielding a 106 nm/pixel. Images were acquired using 488 nm, 561nm and 647 nm (Coherent) laser lines and acquisition was controlled by NIS Elements AR software. To ensure that kinetochore could be tracked overtime with a reduced number of optical sections, cells were imaged under modest cell confinement. An image stack was acquired: every 6 seconds, 9 planes separated by 0.5 µm (Figures 1, 6 and Fig. S1C); 1 min, 11 planes separated by 0.5 µm, Fig. S1A, B); 10 seconds, 9 planes separated by 0.5 µm (Figure 3). Fluorescence intensity of kinetochore Venus-MAD1 was manually tracked throughout mitosis using the image analysis software Fiji 2.16.0 [79]. The recorded image stacks were sum projected and a region was drawn encircling the kinetochore and three different cytoplasmic background sites at each timepoint. MAD1 kinetochore fluorescence intensity (S_{KT}) was calculated by subtracting the averaged

cytoplasmatic signal (S_{BG}), represented in the following equation: $S_{KT, corrected} = S_{KT} - S_{BG, averaged} \times A_{KT}/A_{BG}$ S: raw integrated density; A: Area. The calculated signal intensity was normalized to the followings: the clear last peak of the signal decay curve in untreated/control, mock treated and siHAUS6 conditions; the first frame after adding the inhibitor in MPS1i and CDK1i treatments; the average of the first 10 timepoints in nocodazole treated cells. A single-phase exponential decay function was fitted globally across curves polled from all kinetochores in each experimental condition using the equation: Y = (Y0- Plateau) x (exp^(-Kx)) + Plateau, in GraphPad Prism 9 (Boston, Massachusetts USA). The half decay time ($t_{1/2}$) for each condition was derived from the fit according to $t_{1/2} = \ln(2)/K$. To test for differences in the rate of MAD1 decay (K, derived from the global fit) in untreated vs treated cells or large vs small kinetochores between conditions an extra sum-of-squares F-test was used. Quantification of the signal intensity ratio between kinetochore and cytoplasm (Fig. S1B), was performed manually using Fiji 2.16.0. Three regions were drawn encircling the kinetochore (KT), the cytoplasm (cyto) and an area outside of the cell (background signal, BG) at define time points (anaphase onset, 10, 20, 30 and 40 minutes before anaphase). The kinetochore and cytoplasmic fluorescence intensities were calculated by subtracting background signal, represented in the following equations: $S_{KT, corrected} = S_{KT}/A_{KT} - S_{BG}/A_{BG}$; $S_{cyto, corrected} = S_{cyto}/A_{cyto} - S_{BG}/A_{BG;}$ S: signal; A: Area. The ratio of the corrected kinetochore over cytoplasmatic signals was then calculated. To observe how Mad1 signal spatial distribution within the kinetochore changed throughout time kymographs were produced from live recordings of IM cells (Figure 3). Image stacks were sum projected using Fiji 2.16.0 and kymographs were generated with a custom-written routine in MATLAB (Mathworks, Natick, MA) that compensates for spindle rotation and translations previously described in [64].

<u>Cell confinement</u>

For cell confinement, we adopt a cell confiner as previously described [39, 62] using a custom-designed polydimethylsiloxane (PDMS, RTV615, GE) layout to fit a 35mm diameter fluorodish. A suction cup was custom-made with a 10:1 mixture

(w/w PDMS crosslinker A/ B) and baked on an 80 ºC hot plate for 30mins and left to dry over-night before unmolding. A PDMS confinement slide was then prepared with a 10:1 mixture (w/w PDMS crosslinker A/ B) molded into micropillars with a height of 8 µm (using a SU-8 wafer mold) polymerized onto a 10 mm round coverslip and baked for 95 °C for 15 min. The PDMS confinement slide was attached to the PDMS suction cup and connected to a vacuum generator (AF1-dual, Elveflow).

Quantification of MAD1 intra-kinetochore mobility via fluorescence recovery after photobleaching (FRAP)

For FRAP experiments, IM cells stably expressing Venus-MAD1 were plated on fibronectin coated 35mm FluoroDish (World Precision Instruments, FD35-100) 36-48 h before imaging. To elicit uniform and maximal kineotchore-MAD1 occupancy, cells were treated with nocodazole for 30 minutes before the experiment. To ensure that the bleached kinetochore could be tracked overtime with a reduced number of optical sections, an agar overlay was placed on top of the cells decreasing the cell volume, as described in [63]. Briefly, a 170 µm thick layer of 2% low-melting-point agarose in L15 medium supplemented with 10% FBS was prepared in advance and incubated for 30 minutes with pre-warmed L15 + 10% FBS containing nocodazole. Immediately before imaging, a small piece of the agar layer was gently placed over the cells that were maintained in a minimal amount of medium to prevent cell dehydration while ensuring compression. FRAP experiments were conducted on a Leica Scanning Confocal STELLARIS 8 FALCON (Leica Microsystems, Germany), equipped with an incubation chamber and a power HyD S detector. Cells were imaged with a water-immersion 86x 1.20 NA HC PL APO STED white objective (Leica Microsystems, Germany), plus a 4.5x zoom, yielding an 86 nm/pixel sampling. The 488-nm emission wavelength of a white Light Laser (WLL) was used to bleach MAD1 signal from either part of or an entire kinetochore with 2 pulses of 0.3 seconds each. An image stack of 3 z-planes at a 0.5 µm interval was acquired with the following routine: 3 pre-bleach frames, every 1.3 seconds; kinetochore bleaching; post-bleach 5 frames, every 1.3 seconds for 5 frames, 10 frames,

every 2 seconds and then every 3 seconds for up to 55 seconds. The selected representative images show sum-intensity projections of the image stacks. Venus-MAD1 fluorescence at the kinetochore was manually tracked on the sum projected image stacks using Fiji 2.16.0and a custom-designed script in Python 3.13. Four rectangular ROIS were defined corresponding to: (i) the bleached region of the experiment kinetochore; (ii) the non-bleached region of the experiment kinetochore; (iii) the unperturbed kinetochore from the pair (sister KT) and (iv) a kinetochore from an unperturbed pair (control KT). Additionally, two square ROIs with 0.86 μm sides were drawn over the cytoplasm to measure background fluorescence (BG). A custom-designed script was used to draw the kinetochore ROIs with a constant width of 0.6 μm, and length defined by the distance of the kinetochore extremities in the pre-bleach frame (manually marked based on MAD1 signal using Fiji 2.16.0). In the case of the partially ablated kinetochore the length of the non-bleached region was defined at the first frame post-bleaching, and the length of the bleached region was defined as the difference between the total kinetochore length and the length of the non-bleached region. The long axis of the rectangle was defined based on the vector described by the points marking the extremities of the non-bleached signal and was adjusted at every time point to track the kinetochore motion. MAD1 kinetochore fluorescence intensity ($S_{KT, corrected}$) was corrected for fluctuations in the cytoplasmatic fluorescent signal as described in the following equation: $S_{KT, corrected} = S_{KT} / (a \times time + b)$; S_{KT}: kinetochore MAD1 raw integrated density; a, b: constants provided by a linear fit of the cytoplasmatic MAD1 raw integrated density. The corrected kinetochore signal was then normalized to the average of the 3 pre-bleach values ($S_{KT, normalized}$) and fit to a single exponential association function: Y = Y0 + (Plateau – Y0) x (1-(exp^(-Kx))); Y0 value was constrained to be the $S_{KT, corrected}$ at the first frame post-bleaching. Half recovery time ($t_{1/2}$) was derived from the fit according to $t_{1/2} = \ln(2)/K$. Fluorescence recovery percentage (Recovery) was calculated according to Recovery = (Plateau – Y0) / (1 – Y0). Fitting and downstream statistical analysis was performed using GraphPad Prism 9 (Boston, Massachusetts USA). Cells where bleaching efficiency was < 50%;

focal plane changes were > 1 μm; or where the normalized MAD1 fluorescence could not be fitted to a single exponential (if the 95 % confidence interval for any of the parameters could not be determined) were excluded from the analysis. Line intensity profiles showing Venus-MAD1 signal along the kinetochore were measured from a ROI covering the entire kinetochore length and a width of 0.250 μm at selected times.

Quantification of kinetochore MAD1 signal distribution with Stimulated Emission Depletion (STED) Microscopy

Indian muntjac fibroblasts stably expressing Venus-MAD1 were seeded on glass coverslips and processed as described in the “Immunofluorescence” section. 3D image stacks were acquired using an Abberior 'Expert Line' gated-STED microscope, equipped with a Nikon Lambda Plan-Apo 1.4NA 60x objective lens. CH-STED mode was implemented as described before [62]. Images were acquired using excitation wavelengths at 488 nm, 561 nm, and 640 nm and a single doughnut-shape depletion beam at 775 nm, a 0.8 Airy unit pinhole and the STED channel had a time-gate threshold of 500 ps. Pixel size was set to 30 nm in xy and 200 nm in z and Image stacks covering near full spindle volume (~8 μm). The selected representative images show sum-intensity projections of a fraction of the Z-slices (5-10). In images that show merged channels, histograms were cropped to allow visualization of all structures. Venus-MAD1 and tubulin signal distribution was analyzed along individual kinetochores in sum projected 3D stacks (5-10 slices) using Fiji 2.16.0. A line of 0.6 μm width was drawn along the longitudinal axis of the kinetochore (defined by the ACA signal). Intensity line profiles were extracted along the kinetochore for both MAD1 and tubulin channels and background subtracted (average cytoplasmatic intensity value). Corrected signal intensity was normalized to the maximum intensity value within each kinetochore. To visualize and measure correlations between MAD1 and tubulin signals, we calculated the intensity z-scores, standardized internally (for each kinetochore). Each position along the kinetochore is represented as a point in a 2D space where the z-scores are the x-y axes and an ensemble of

720 kinetochores was either overlaid in the same scatter plot or displayed and
721 calculated for isolated kinetochores. The product zMAD1.ztubulin at each data
722 point is the local contribution to an overall correlation. Averaging over all data
723 points yields the covariance normalized to the standard deviation product, known
724 as the Pearson correlation coefficient. The Matlab function *corrcoef* was used,
725 which calculates Pearson's correlations and p-values with a two-tailed Student
726 t-test for zero correlation. 3D reconstructions of the image stacks were obtained
727 with Imaris 9.3.1 (Oxford Instruments).
728
729 Laser microsurgery and correlative live-cell confocal and fixed-cell CH-STED
730 microscopy
731 Indian muntjac cells expressing 2x-GFP-CENP-A and GFP-CENTRIN-1 and
732 mScarlet-MAD1 were seeded on fibronectin coated 25 mm, no. 1.5, round
733 coverslips (CAT 10593054, fisher scientific) 48h prior to the experiment. To
734 induce mScarlet-MAD1 expression, cells were incubated with 1 ug/mL of
735 doxycycline for 24h. Before imaging the coverslips were mounted on a 35 mm
736 Attofluor™ Cell Chamber (CAT A7816, Invitrogen) and the media replaced with in
737 Leibovitz's L15 medium (GIBCO, Life Technologies) supplemented with 10%
738 FBS. Cells were imaged using Nikon-Ti spinning-disk confocal microscope with a
739 100x 1.4 NA oil objective as detailed in the "Monitoring kinetochore MAD1 levels
740 in live recordings" section. Cells in metaphase were identified by having MAD1
741 negative kinetochores aligned at the equator and increased inter- kinetochore
742 and pole-pole distance (assessed by GFP-CENTRIN-1). After recording a
743 pre-surgery image stack, one of the large kinetochores (from the IM chromosome
744 3+X) was partially ablated with a 532 nm laser, controlled by a custom routine. A
745 detailed description of the microsurgery setup can be found in [80]. 2-5 consecutive
746 pulses with a 0.35 µm step and a 12 Hz repetition rate) were applied. The pulse
747 width was 10 ns and the pulse energy was 3.9–4.4 µJ. After surgery an image
748 stack (5 planes, 0.75 µm z-step) was recorded every minute until MAD1 signal
749 was detected at the kinetochore, for up to 30 min; after MAD1 detection the
750 acquisition routine was changed: 7 planes, 0.5 µm z-step every 20 seconds for

751 5 min. As a control for uniform MAD1 signal distribution, non-ablated cells were
752 imaged upon acute nocodazole treatment (5 to 60 min incubation). For
753 correlative live-cell confocal and fixed CH-STED microscopy analysis, once
754 MAD1 signal was detected at the kinetochore a fixation solution was added to the
755 imaging chamber. The location of the cell of interest was marked with a
756 laser-engraved pattern on the glass coverslip. The sample was processed for
757 staining as described in the “Immunofluorescence” section. After locating the
758 surgery cell with a 10x objective, a super-resolved image stack of the spindle was
759 acquired with CH-STED as described in the “Quantification of kinetochore MAD1
760 signal distribution with Stimulated Emission Depletion (STED) Microscopy”
761 section (pixel size 35 nm in xy and 150 nm in z). Representative images show a
762 sum (live-cell data) or max-intensity (fixed-cell data) projection of all z-slices that
763 contain the kinetochore of interest. Histograms were adjusted per frame to allow
764 better visualization of the representative phenotypes. To measure MAD1
765 recruitment after laser microsurgery, kinetochores were manually tracked using
766 the GFP-tagged CENP-A as a reference in Fiji 2.16.0. kinetochore deformation
767 was defined as the first time point when an increase in the angle between the line
768 connecting the ends of the surgery kinetochore and the line connecting the ends
769 of the unperturbed kinetochore from the pair (sister kinetochore) was observed.
770 MAD1 recruitment was defined as the first time point when mScarlet-MAD1
771 signal was visible at the sister kinetochore. MAD1 signal distribution along the
772 sister kinetochore was measured at the time point when signal intensity appeared
773 highest, based on visual assessment. On the cells where correlative live-cell
774 spinning-disk confocal and CH-STED microscopy was performed, tubulin signal
775 distribution was measured in the fixed sample. Measurements were performed
776 on sum projected stacks containing the kinetochore pair of interest. A segmented
777 line of 0.8 µm width (for MAD1, live imaging) or 0.9 µm width (for tubulin, fixed cell
778 imaging) was drawn to span the full length of the kinetochore, as defined by the
779 CENP-A signal, starting from the end that retained its counterpart (or randomly in
780 nocodazole treated cells). Intensity line profiles were extracted along the
781 kinetochore for all channels and background subtracted (cytoplasmatic signal

near the kinetochore). The corrected intensity profile was normalized to the maximum within each kinetochore, as exemplified for CENP-A: $S_{CENP\text{-}A,\ norm}$ = ($S_{CENP\text{-}A}$ - $S_{BG\ CENP\text{-}A}$) / max ($S_{CENP\text{-}A}$ - $S_{BG\ CENP\text{-}A}$), S: mean pixel intensity. To correct for intensity variations caused by kinetochore deformation or movement, intensity profiles are shown as a ratio of MAD1/tubulin over CENP-A. Kinetochore length was normalized to a relative scale ranging from 0 (start of the line profile) to 1 (end of the line profile). The average MAD1/CENP-A ratio intensity profile for each condition (Nocodazole vs Surgery), was calculated using the 'Multiple average curves' function with linear interpolation on OriginPro 2022 (OriginLab Corporation, Northampton, MA, USA). The coefficient of variation of the MAD1/CENP-A ratio was calculated as the standard deviation of the MAD1/CENP-A intensity values along each kinetochore, divided by their mean. Cells that failed to recruit MAD1 within the mean recruitment time + 1 s.d. (~12 minutes) or exhibited only very faint MAD1 signal were excluded from the MAD1 distribution analysis. Statistical analysis and plots were done using GraphPad Prism 9 (Boston, Massachusetts USA).

<u>Quantification of kinetochore MAD1 levels in prometaphase and metaphase HAUS6 depleted cells</u>

Control and HAUS6 depleted cells expressing Venus-Mad1 were treated with MG 132 for 1h and then fixed and stained for as detailed in the "Immunofluorescence for wide-field" section. Samples were imaged on AxioImager Z1 equipped with a CCD camera (ORCA-R2, Hamamatsu) operated by Zen software (Carl Zeiss, Inc.). 3D image stacks covering the entire cell volume (0.23 µm z-step) were acquired using a 100× Plan-Apochromatic oil differential interference contrast objective lens, 1.46 NA (Carl Zeiss Microimaging Inc.) and excitation wavelengths at 488 nm, 561 nm, and 640 nm. The number of cells with MAD1 positive kinetochores was visually assessed for each condition. Kinetochore Venus-MAD1 signal intensity was measured on a single focal plane using Fiji 2.16.0. Cytoplasmatic Venus-MAD1 signal was averaged from 3 regions outside the spindle area. The ration between kinetochore and cytoplasm signal was calculated according to the equation: S_{KT} / $S_{cytoplasm;}$ S: mean pixel intensity.

Statistical analysis and plots were done using GraphPad Prism 9 (Boston, Massachusetts USA).

Cell tracking and daughter fate analysis in live recordings

Indian muntjac fibroblasts stably expressing GFP-H2B were plated on fibronectin coated µ-Slide 4 Well Glass Bottom (Ibidi GmbH, 80427) with Ham's F-10 media supplemented with 20% FBS 24h before imaging. Cells were recorded using the Zeiss LSM 980 Airyscan confocal microscope built on an Axio Observer 7 inverted stand with a motorized piezo stage and active focus stabilization. A controlled atmosphere chamber (CO2 and temperature) was used. Objective lens was a dry 0.3NA 10x Plan Neofluar. Detection was performed with two GaAsP detectors. Image acquisition was carried out with ZEN 3.11 software. 3D image stacks (pixel size 830 nm in xy, 4 planes separated by 6.7 µm, pinhole Airy unit of 1.23, scan speed of 7, no averaging) were recorded every 7 min using both transmitted light and an excitation wavelength at 488 nm. In experiments where mitotic delay was induced through monastrol treatment, cells were imaged in the presence of the drug for 6h before washing out the drug. The fate of cell families was tracked for 72h. In experiments where HAUS6 was depleted, cells were treated with control or HAUS6 siRNAs shortly before imaging. Cell families were then tracked for 96h. Cells were tracked manually using TrackMate [81]. Single-cell lineages and cell cycle durations (frame of anaphase mother cell to frame anaphase daughter cell) were analysed by modifying previously published [82] Jupyter notebooks (7.0.8). We defined mitotic duration as the frame of mitotic onset (condensing chromatin) until the first frame of anaphase (clearly separated daughter chromatin). For each division event, we determined mitotic defects and errors, and the fate of the daughters. For downstream analysis, filtering and plotting, all data were integrated using Jupyter notebooks (Python 3.12) and the pandas (2.2.2) [83] and Altair (5.4.1) [84] libraries. Fiji/ImageJ [79] macros and analytical code for the daughter fate analysis is available at https://github.com/TobiasKletter/MitoticStop.

Co-immunoprecipitation

Indian muntjac fibroblasts stably expressing GFP-H2B were grown on with Ham's F-10 media supplemented with 20% FBS. To obtain a mitotic arrested population cells were treated for 16h with 3.3 µM Nocodazole. 10 million mitotic cells were collected by shake-off. The remaining interphase cells (NOC interphase) and cells left untreated (asynchronous) were collected by cell scrapping. Cells were pelleted at 300 g for 5 minutes, washed with cold PBS and cell pellets were snap frozen in liquid nitrogen. Co-immunoprecipitation assay was optimized from the protocol described in [29]. Cell were resuspended in lysis buffer (20 mM Tris/HCl, pH 7.5; 50 mM NaCl; 0.5% Triton X-100; 5 mM EGTA; 1 mM dithiothreitol; 2 mM $MgCl_2$; Pierce Protease and Phosphatase inhibitor mini tablets, EDTA-free [Thermo Fisher Scientific; A32961]) and incubated for 45 minutes at 4ºC with agitation. Cell lysates were centrifuged at 15 000 rpm for 5 minutes at 4ºC to collect the supernatant. Protein concentration was quantified and a lysate solution containing 1.5 mg of protein in 1 mL of lysis buffer was prepared for each condition. Lysates were incubated with 3 ug of anti-53BP1 antibody (Novus, NB100-304) or control rabbit IgG for 2h at 4ºC with agitation and subsequently with 20 µL of pre-washed (4x with lysis buffer) Pierce™ Protein A Magnetic Beads (Thermo Fisher Scientific, 88845) for 1h at 4ºC with agitation. The non-binding supernatant faction was collected and the beads were washed 4x with lysis buffer. The bound fraction was eluted from the beads by resuspending in 2x sample buffer (50 mM Tris-HCl, pH 6.8, 2% SDS, 10% glycerol, 1% β-mercaptoethanol, 12.5 mM EDTA, and 0.02% bromophenol blue) and denatured at 95 °C for 5 min. Samples were analyzed through western blot.

<u>Western blotting</u>

Protein samples of 13-20 ug in sample buffer were loaded on a 4–15% Mini-PROTEAN® TGX™ Precast Protein Gel (Bio-Rad, 4561084), mounted on a Mini-PROTEAN vertical electrophoresis apparatus (Bio-Rad). NZYColour Protein Marker II (NZYTech) was used as a ruler. Blotting was performed with a Transfer-Blot Turbo transfer system (Bio-Rad) onto 0.2 µm Nitrocellulose membranes. Membranes were blocked in blocking buffer (5% powder milk in PBS Tween 0.1%) for 1h. Anti-53BP1 rabbit 1:1000 (Novus, NB100-304),

anti-USP28 rabbit (Abcam, ab126604), anti-p53 DO-1 mouse (Santa Cruz Biotechnology, SC-126) and anti-GAPDH mouse 1:10 000 (Proteintech, 60004-1-Ig) primary antibodies were diluted in blocking buffer and incubated 1 h (4 °C) with agitation. Anti-rabbit HRP (Jackson ImmunoResearch, 111-035-003) and anti-mouse light chain specific HRP (Jackson ImmunoResearch, 115-035-174) secondary antibodies were diluted 1:5000 in blocking buffer and incubated 1 h (4 °C) with agitation. Membranes were developed with Clarity Western ECL Blotting Substrate (Bio-Rad, 1705061) and detected in the Chemidoc XRS system and Image Lab software (Bio-Rad).

Acknowledgements

We would like to thank all colleagues that generously provided reagents used in this study, and Paula Sampaio and Maria Azevedo from i3S Advanced Light Microscopy Facility for technical support. We are indebted to Franz Meitinger for critical discussions and technical advice on the mitotic stopwatch. We also thank CID Lab members for discussions and constructive feedback throughout the course of this project, with special thanks to Daniela Andrade and Rui Martins for their strong contribution during mitotic shake-offs. NO, JS-O and EW were respectively supported by fellowships SFRH/BPD/118126/2016, SFRH/BD/07730/2021 and 2022.13008.BD from Fundação para a Ciência e a Tecnologia of Portugal. This project was funded by The European Union through the European Research Council grant KAREVO (project 101140624) to HM.

Author contributions

Conceptualization: HM

Methodology: NO, JS-O, TK, AJP, EW

Investigation: NO, JS-O, TK

Visualization: NO, JS-O, TK, AJP

Funding acquisition: HM

Project administration: HM

Supervision: HM, AJP

Writing – original draft: NO, HM

Writing – review & editing: NO, JS-O, TK, AJP, EW, HM

Competing interests

Authors declare that they have no competing interests.

Figure legends

Figure 1. SAC protein MAD1 is gradually removed from the kinetochore in a microtubule and mitotic kinases dependent manner.

(A) Representative live-cell recording images of Indian muntjac fibroblasts expressing Venus-MAD1 (orange) and with SiR-tubulin labeled microtubules (grey). Scale bar: 5µm.

Insets highlight an early congressing kinetochore pair (dashed square) and dashed circles show polar kinetochores/chromosomes. Scale bar: 5µm.

(A') Insets focusing on 1 half-spindle to highlight the congression of polar chromosomes (dashed circles) from A. Scale bar: 5µm.

(A'') Kymographs depicting Venus-MAD1 signal of the 2 polar chromosomes shown in A'. The closest pole position is shown by the dashed line. Leading (black asterisk) and trailing kinetochore (white asterisk) and indicated for each pair. Scale bar: 5µm.

(B) Representative live-cell recording images of Indian muntjac fibroblasts acutely treated with Nocodazole, MPS1 and CDK1 inhibitors. Venus-MAD1 (orange) and SiR-tubulin labeled microtubules (grey). Insets highlight a kinetochore pair. Scale bar: 5µm.

(C) Normalized Venus-MAD1 fluorescence decay IM cells untreated (control) or treated with Nocodazole, MPS1 and CDK1 inhibitors. Data represented as mean ± 95% confidence interval (CI; Control n = 53 kinetochores, 7 cells, green; Nocodazole n = 31 kinetochores, 8 cells, grey; MPS1i n = 63 kinetochores, 12 cells, yellow; CDK1i n = 18 kinetochores, 10 cells, blue; data pooled from at least five independent experiments per condition).

(D) Normalized Venus-MAD1 fluorescence decay in large or small kinetochores from untreated cells. Data are represented as mean ± 95% CI. (Large KTs n = 19 kinetochores, 7 cells, 5 independent experiments, dark green; small KTs n = 34 kinetochores, 5 cells, 4 independent experiments, light green).

(E) Summary table of the parameters extracted from a single exponential fitting of Venus-MAD1 fluorescence decay across the condition shown in C and D. P-values were calculated using extra sum-of-squares *F*-test comparing the rate

of MAD1 decay (K, derived from global fit) in untreated vs treated cells or large vs small kinetochores.

Figure 2. MAD1 is immobile within kinetochores

(A) Schematic representation of Dynein-mediated MAD1/MAD2 complex removal from kinetochores.

(A') Predicted curves of MAD1 fluorescence recovery after partial kinetochore bleaching assuming MAD1 to be mobile (left) or immobile (right) within the kinetochore. Lines represent the fluorescence levels from the region of the kinetochore that was bleached (light blue) or left unperturbed (dark blue).

(B), (C) Representative images of Indian muntjac cells pre- and post-bleach of part (B) or an entire kinetochore (C). Insets: kinetochore pair that was perturbed. Dashed line boxes indicate the ablated kinetochore region (partial bleach KT: non-bleached region - dark blue; bleached region – blue; total bleach KT - yellow).

(B'), (C') Venus-Mad1 signal intensity profile along the kinetochore at pre-bleach and at selected times post-bleach for kinetochores shown in B and C, respectively.

(B''), (C'') Normalized Venus-Mad1 fluorescence recovery curves for cells shown in B and C, respectively (Dark blue line non-bleached region; light blue bleached region; yellow line totally bleached kinetochore; black and dark grey lines unperturbed kinetochores from the bleach or a control kinetochore pair, respectively; light grey cytoplasm; from fit curves are shown by the semi-translucid line).

(D) Kinetochore Venus-MAD1 fluorescence recovery after partial or total kinetochore bleach (Partial KT bleach n = 7; total KT bleach n = 8 from at least two independent experiments). Dots show individual kinetochores. P = 0.2319, Mann-Whitney test (two-tailed).

(E) Half recovery times of kinetochore Venus-MAD1 fluorescence after partial or total kinetochore bleach. Dots show individual kinetochores. P = 0.5358, Mann-Whitney test (two-tailed).

Figure 3. MAD1 removal along an individual kinetochore is not uniform

(A) Live-cell recording images of Indian muntjac fibroblasts stably co-expressing Venus-MAD1 (orange) and mScarlet-CENP-A (blue) with SiR-tubulin labeled microtubules (grey). Inset: kinetochore pair that shows non-uniform loss of MAD1 signal. Dashed arrow indicates the kinetochore depicted in B. Scale bar: 5µm.

(B) Kymographs depicting Venus-MAD1 and mScarlet-CENP-A signal distribution along the longitudinal axis of the kinetochore shown in A. Each channel is shown on a greyscale and as a heatmap. Scale bar: 1µm

Figure 4. MAD1 removal along individual kinetochores correlates with local microtubule density

(A) Representative CH-STED image of an Indian muntjac fibroblasts with partially attached kinetochores. Microtubules (grey; STED), centromeres (ACA; blue; STED) and Venus-MAD1 (orange; confocal). Insets: partially attached kinetochore. Scale bar: 2µm.

(B) Three-dimensional reconstruction of the cell shown in A (different perspective). Inset: partially attached kinetochore. The kinetochore pair of interest is traced by a dashed line. Microtubules (grey), centromeres (ACA; blue) and Venus-MAD1 (orange). Scale bars, Left: 3µm; Right: 1µm.

(C) Max normalized Venus-Mad1 (orange) and tubulin (microtubules; grey) signal intensity profile along the longitudinal axis of the kinetochore highlighted in A (arrowhead).

(D) Pearson correlation coefficient between MAD1 and microtubules signal intensity along the kinetochore. Bars show individual partially attached kinetochores (n=21 kinetochores, 7 independent experiments).

E) Representative distribution of kinetochore sub-regions showing positive, negative and no correlation between MAD1 (y-axis) and microtubules (x-axis) intensity z-scores. Dots represent distinct positions along the “kinetochore” shown below the graphs. NE and SW quadrants contribute positively, while NW and SE quadrants contribute negatively to the Pearson correlation coefficient (r).

(F) Correlation map of MAD1 and microtubule intensity z-scores for the

kinetochores shown in D. The underlying scatterplot contains data from multiple kinetochores, with each dot representing a sub-kinetochore region. For visualization, the scatterplot was converted into a regional density map. P-value was calculated with Student t-test for zero correlation (two-sided).

Figure 5. Local perturbation of kinetochore structure results in a localized SAC response that inversely correlates with microtubule occupancy

(A) Schematic summary of the kinetochore response to partial laser microsurgery ablation.

(B) Representative live-recording images of Indian muntjac cells expressing 2x-GFP-CENP-A and GFP-CENTRIN-1 (both in blue) and mScarlet-MAD1 (orange/ grey scale) upon partial kinetochore surgery or acute Nocodazole treatment. Insets: kinetochore pair that was perturbed. Arrows point to the ablated kinetochore region, pre- and post-surgery (solid and hollow arrow, respectively). Arrowheads show MAD1 recruitment. Scale bar: 2µm.

(B') Max normalized line intensity profile plot of MAD1/CENP-A signal ratio along the longitudinal axis of the kinetochores highlighted in A (surgery cell in orange; nocodazole cell in grey).

(C) Dot plot showing the time from surgery to observable deformation (bending; n= 12 kinetochores) and MAD1 signal re-appearance (n = 14 kinetochores) at the sister kinetochore in cells where SAC recruitment was observed. Each dot represents an individual kinetochore from a different cell, recorded during 13 independent experiments. $P < 0.0015$, Wilcoxon matched-pairs signed rank test.

(D) Max normalized MAD1/CENP-A ratio intensity profile along the longitudinal axis of kinetochores after partial surgery of their sisters (orange) or upon acute Nocodazole treatment (NOC; grey). Thin lines show individual kinetochores and thick lines show average curves (surgery n = 11 kinetochores/cells, 10 independent experiments; Nocodazole n = 19 kinetochores/cells, 2 independent experiments). The graph depicts a cohort of cells that recruit MAD1 to the proximal tip of the kinetochore, relative to the surgery region (n = 11/16 MAD1 recruiting kinetochores).

(E) Coefficient of variation of MAD1/CENP-A signal ratio along kinetochores

after partial surgery of their sisters. Dots represent individual kinetochores pooled from all cells where MAD1 recruitment was observed (surgery n = 16 cells, 14 independent experiments; Nocodazole n = 19 cells, 2 independent experiments). P <0.0001, Mann-Whitney test.

(F), (F') Representative images from correlative live cell spinning disk (F) and fixed CH-STED microscopy (F'). Indian muntjac cells expressing 2x-GFP-CENP-A and GFP-CENTRIN-1 (both in blue) and mScarlet-MAD1 (orange/grey scale) were fixed after partial kinetochore surgery and stained to visualize microtubules (grey). Insets: kinetochore pair that was perturbed. Arrows point to the ablated kinetochore region, pre- and post-surgery (solid and hollow arrow, respectively). Arrowheads show MAD1 recruitment. Scale bar: 2µm.

(F'') Max normalized line intensity profile plot of MAD1/CENP-A (live cell data just before fixation, orange) and microtubules/CENP-A (fixed cell data, grey) signal ratio along the longitudinal axis of the kinetochore highlighted in F and F'.

Figure 6. Partial microtubule occupancy at kinetochores after Augmin depletion delays MAD1 removal and SAC silencing

(A) Representative live-cell recording images of Indian muntjac fibroblasts mock or HAUS6 siRNA treated. Venus-MAD1 (orange) and SiR-tubulin labeled microtubules (grey). Scale bar: 5µm.Insets highlight a kinetochore pair. Asterisks indicate the two kinetochores from the pair. Scale bar: 5µm.

(B) Normalized Venus-MAD1 fluorescence decay from A. Data from at least five independent experiments are represented as mean ± 95% confidence interval (Mock n = 48 kinetochores, 10 cells, grey; siHAUS6 n = 47 kinetochores, 10 cells, blue).

(C) Summary table of the parameters extracted from a single exponential fitting of Venus-MAD1 fluorescence decay across the conditions shown in B. P-values were calculated using extra sum-of-squares *F*-test comparing the rate of MAD1 decay (K, derived from global fit) in mock vs siHAUS6 treated cells.

(D) Percentage of cells with at least one MAD1 positive kinetochore in mock (grey) or siHAUS6 (blue) treated cells after 1h of MG132 arrest. Bars show

mean, error bars show s.d. from three independent experiments (n≥293 cells per condition). P <0.0001, prometaphase; P=0.0008, metaphase; unpaired t test (two-sided).

(E) Dot plot showing the ratio between kinetochore and cytoplasmatic Venus-MAD1 signal intensity in mock (grey) or siHAUS6 (blue) treated cells fixed after 1h of MG132 arrest. Dots show individual kinetochores, bars show mean, error bars show s.d. from three independent experiments (n ≥ 309 kinetochores, ≥ 17 cells per condition). P<0.0001, Mann-Whitney test (two-sided).

(F) Representative CH-STED image of an Indian muntjac control or HAUS6 depleted cells treated with MG132 for 1h. Microtubules (grey; STED), centromeres (ACA; blue; STED) and Venus-MAD1 (orange; confocal). Inset: full (control) or partially (siHAUS6) attached kinetochore pair. Scale bar: 2µm.

Figure 7. Delayed SAC silencing due to partial microtubule occupancy at kinetochores activates the mitotic stopwatch to stop cell proliferation

(A) Schematic summary of the experimental setup and downstream analysis.

(A') Mitotic duration of Indian muntjac cells expressing H2B-GFP with decreasing HAUS6 levels (time in the presence of control or HAUS6 siRNA; grey and blue, respectively). Data pooled from three independent experiments (siHAUS6 n = 370, siCtrl n = 335). Circles denote mean in each time bin (bin size = 12h), error bars show the s.e.m.

(B) Bar graph showing the percentage of Indian muntjac cells that exited mitosis with a particular mitotic defect/ error at decreasing HAUS6 levels. Data pooled from three independent experiments (n = 469 cells). Bars show mean in each time bin (bin size = 6h or 24h), error bars show the s.e.m.

(C) Plot of the mitotic cell fate as a function of mitotic duration in Indian muntjac cells treated with siHAUS6 for 0 to 96h. Bars show individual cells (n = 469 cells pooled from three independent experiments).

(D) Plot of daughter cells fate (Gen 2) as a function of mother cell mitotic duration (Gen 1). Only mother cells from the selected cohort (12-36h of siHAUS6 treatment) are shown. Bars show individual daughter cells (n = 272 cells pooled

from three independent experiments).

(E) Bar graph showing the percentage of mother cells from the selected cohort that has 0, 1 or 2 daughter cells dividing at least once, as a function of mother cells time in mitosis. Only mother cells from the selected cohort (12-36h of siHAUS6 treatment) and that completed mitosis with no defects are shown. Data are binned (< 30 min n = 1 cell, 30-60 min n = 25 cells, 60-90 min n = 33 cells, 90-120 min n = 27 cell, > 120 min n = 10 cells pooled from three independent experiments).

(G) Analysis of 53BP1 immunoprecipitates from Indian muntjac fibroblast populations treated with nocodazole (3.3 µM) for 16 h. Cells were separated into interphase and mitotic cells via mechanical shake-off. As negative control, rabbit IgG were used. GAPDH as loading control.

(H) Immunoblot on whole-cell lysates from human RPE1 hTERT cells and Indian muntjac fibroblasts (GFP-H2B), that were treated for 16h either with DMSO, etoposide (5 µM), or nocodazole (3.3 µM, mitotic shake-off) and probed for p53 enrichment. GAPDH as loading control.

Figure 8 - Microtubule occupancy at kinetochores integrates with the mitotic stopwatch to ensure faithful daughter cell proliferation

(Top) Augmin-mediated K-fiber maturation promotes maximal microtubule occupancy at kinetochores through gradual and highly localized MAD1/MAD2 removal, resulting in timely SAC silencing. In this way, mitotic timing is optimal, fidelity is maintained, and daughter cells continue proliferating.

(Bottom) When K-fiber maturation is impaired, for example through disruption of Augmin-mediated microtubule amplification, microtubule occupancy at kinetochores remains partial and SAC silencing is delayed. Eventually, the cell divides either after achieving full occupancy or while kinetochores are still only partially occupied. The resulting mitotic delay is registered by the mitotic stopwatch, which bookmarks daughter cells to halt proliferation.

Supplemental Figure legends

Figure S1. MAD1 is undetectable at kinetochores 20 minutes before anaphase

(A) Representative live-cell recording images of Indian muntjac fibroblasts expressing Venus-MAD1 (orange, upper panels or grey, lower panels) and mScarlet-CENP-A with SiR-tubulin labeled microtubules (grey, upper panels). Scale bar: 5µm.

(B) Dot plot showing the ratio between kinetochore and cytoplasmatic Venus-MAD1 signal intensity at selected time points. Dots show individual kinetochores, lines show mean ± s.d. (-40 min: 87 kinetochores, $p< 0.0001$; -30 min: 123 kinetochores, $p< 0.0001$; -20 min: 137 kinetochores, $p> 0.9999$; -10 min: 126 kinetochores, $p> 0.9444$; Anaphase onset: 126 kinetochores; 15 cells from 7 independent experiments)., P value calculated with Kruskal-Wallis test with Dunn's comparisons of mean fluorescence in each time point with anaphase onset.

(C) Normalized signal intensity of cytoplasmatic Venus-MAD1 throughout live cell recording. Lines show selected cytoplasmatic regions (n= 27 spots, 9 cells, 6 independent experiments).

Figure S2. MAD1 tracking on individual kinetochores throughout mitosis

Single kinetochore tracks of Venus-MAD1 fluorescence decay shown in Figure 1 and 6. Thin lines represent individual kinetochores (Control n = 53 kinetochores, 7 cells, green; Control Large KTs n = 19 kinetochores, 7 cells, dark green; Control small KTs n = 34 kinetochores, 5 cells, light green; Nocodazole n = 31 kinetochores, 8 cells, grey; MPS1i n = 63 kinetochores, 12 cells, yellow; CDK1i n = 18 kinetochores, 10 cells, blue; Mock n = 48 kinetochores, 11 cells, light grey; siHAUS6 n = 47 kinetochores, 10 cells, purple blue; data pooled from at least four independent experiments per condition). Thick lines show the single-phase exponential decay fit curve for all pooled data (except for Nocodazole: average cure curve).

Figure S3. Additional examples of partially attached kinetochores

(A), (A) Representative CH-STED image of Indian muntjac fibroblasts with partially attached kinetochores. Microtubules (grey; STED), centromeres (ACA; blue; STED) and Venus-MAD1 (orange; confocal). Insets: partially attached kinetochores. Scale bar: 2µm.

(A'), (B') Max normalized Venus-Mad1 (orange) and tubulin (microtubules; grey) signal intensity profile along the longitudinal axis of the kinetochores highlighted in A and B, respectively (arrow head).

(C) Correlation map of MAD1 and microtubule intensity z-scores for the all partially attached kinetochores analyzed in untreated cells. Each scatterplot contains data from a single kinetochore, with each dot representing a sub-kinetochore region. P-value was calculated with Student t-test for zero correlation (two-sided).

Figure S4. Additional examples of localized MAD1 recruitment upon kinetochore laser ablation

(A) Representative live-recording images of Indian muntjac cells expressing 2x-GFP-CENP-A and GFP-CENTRIN-1 (both in blue) and mScarlet-MAD1 (orange/ grey scale) upon partial kinetochore surgery. Insets: kinetochore pair that was perturbed. Arrows point to the ablated kinetochore region, pre- and post-surgery (solid and hollow arrow, respectively). Arrowhead shows MAD1 recruitment. Scale bar: 2µm.

(A') Max normalized line intensity profile plot of MAD1/CENP-A signal ratio along the longitudinal axis of the kinetochore highlighted in A.

(B) Max normalized MAD1/CENP-A ratio intensity profile along the longitudinal axis of kinetochores after partial surgery of their sisters (orange) or upon acute Nocodazole treatment (NOC; grey). Thin lines show individual kinetochores and thick lines show average curves (surgery n = 5 kinetochores/cells, 5 independent experiments; Nocodazole n = 19 kinetochores/cells, 2 independent experiments). The graph depicts a cohort of cells that recruit MAD1 to a distal position relative to the surgery region (n = 5/16 MAD1 recruiting kinetochores). Data from Nocodazole treated cells is the same as shown in Figure 5.

(C), (C') Representative images from correlative live cell spinning disk (C) and fixed CH-STED microscopy (C') in a cell that recruited MAD1 to distal position relative to the surgery region. Indian muntjac cells expressing 2x-GFP-CENP-A and GFP-CENTRIN-1 (both in blue) and mScarlet-MAD1 (orange/grey scale) were fixed after partial kinetochore surgery and stained to visualize microtubules (grey). Insets: kinetochore pair that was perturbed. Arrows point to the ablated kinetochore region, pre- and post-surgery (solid and hollow arrow, respectively). Arrowheads show MAD1 recruitment. Scale bar: 2µm.

(C'') Max normalized line intensity profile plot of MAD1/CENP-A (live cell data just before fixation, orange) and microtubules/CENP-A (fixed cell data, grey) signal ratio along the longitudinal axis of the kinetochore highlighted in C and C'.

Figure S5. Uniform perturbation of microtubule occupancy upon Augmin depletion

(A) Representative CH-STED image of an Indian muntjac fibroblasts with partially attached kinetochores upon siHAUS6 treatment. Microtubules (grey; STED), centromeres (ACA; blue; STED) and Venus-MAD1 (orange; confocal). Insets: partially attached kinetochore. Scale bar: 2µm.

(B) Three-dimensional reconstruction of the cell shown in A. Inset: partially attached kinetochore. The kinetochore pair of interest is traced by a dashed line. Microtubules (grey), centromeres (ACA; blue) and Venus-MAD1 (orange). Scale bars, Left: 3µm; Right: 1µm.

(C) Max normalized Venus-Mad1 (orange) and tubulin (microtubules; grey) signal intensity profile along the longitudinal axis of the kinetochore highlighted in A (arrow head).

(D) Pearson correlation coefficient between MAD1 and microtubules signal intensity along the kinetochore. Bars show individual partially attached kinetochores in siHAUS6 treated cells (n=13 kinetochores, 9 cells, 2 independent experiments).

(E) Correlation map of MAD1 and microtubule intensity z-scores for kinetochores in control (data from Figure 3) and in siHAUS6 treated cells (shown in D). The underlying scatterplot contains data from multiple kinetochores, with each dot

representing a sub-kinetochore region. For visualization, the scatterplot was converted into a regional density map. P-value was calculated with Student t-test for zero correlation (two-sided).

Figure S6. Additional examples of partially attached kinetochores in Augmin depleted cells

(A), (A) Representative CH-STED image of Indian muntjac fibroblasts siHAUS6 treated with partially attached kinetochores. Microtubules (grey; STED), centromeres (ACA; blue; STED) and Venus-MAD1 (orange; confocal). Insets: partially attached kinetochores. Scale bar: 2µm.

(A'), (B') Max normalized Venus-Mad1 (orange) and tubulin (microtubules; grey) signal intensity profile along the longitudinal axis of the kinetochores highlighted in A and B, respectively (arrowhead).

(C) Correlation map of MAD1 and microtubule intensity z-scores for the all partially attached kinetochores analyzed in siHAUS6 cells. Each scatterplot contains data from a single kinetochore, with each dot representing a sub-kinetochore region. P-value was calculated with Student t-test for zero correlation (two-sided).

Figure S7. Extended mitosis activates the mitotic stopwatch to stop cell proliferation in Indian muntjac cells

(A) Schematic summary of the experimental setup and downstream analysis.

(B) Daughter cell cycle duration as a function of mother mitotic duration in Indian muntjac cells expressing H2B-GFP upon monastrol-induced arrest and release. Bars show individual daughter cells (n = 305 cells pooled from two independent experiments). Note that only daughter cells that entered mitosis during imaging were included in the graph (see methods section).

(C) Mitotic duration of Indian muntjac cells that enter mitosis within a given recording time bin. Data pooled from two independent experiments (n = 489). Circles denote mean in each time bin (bin size = 6h), error bars show the s.e.m.

(D) Bar graph showing the percentage of Indian muntjac cells that exited mitosis

with no defects or a particular mitotic defect/ error after distinct mitotic durations (bin size = 30 min). Only mother cells from the selected cohort (0-18h of imaging) are shown. Data pooled from two independent experiments (n = 142 cells). Bars show mean in each time bin (bin size = 6h or 24h), error bars show the s.e.m.

(E) Daughter cells fate (Gen 2) as a function of mother cell mitotic duration (Gen 1). Only mother cells from the selected cohort (0-18h of imaging) and that completed mitosis with no defects are shown are shown. Bars show individual cells (n = 123 cells pooled from two independent experiments).

(E') Percentages of cell families dividing only once (Gen 1 mothers only) versus a second (Gen 2 daughters) or a third time (Gen 3 daughters), after binning the cell families by mitotic duration of the Gen 1 mother. Circles show the two independent experiments, bars show the mean and errors show the s.e.m.

(F) Summary of the percentage of daughter cells that arrest as a function of mother cell mitotic duration and cause of mitotic delay.

References

1. Bakhoum, S.F., and Cantley, L.C. (2018). The Multifaceted Role of Chromosomal Instability in Cancer and Its Microenvironment. Cell *174*, 1347-1360. 10.1016/j.cell.2018.08.027.
2. Rieder, C.L., Cole, R.W., Khodjakov, A., and Sluder, G. (1995). The checkpoint delaying anaphase in response to chromosome monoorientation is mediated by an inhibitory signal produced by unattached kinetochores. The Journal of cell biology *130*, 941-948.
3. Musacchio, A., and Salmon, E.D. (2007). The spindle-assembly checkpoint in space and time. Nature reviews *8*, 379-393. nrm2163 [pii] 10.1038/nrm2163.
4. Lara-Gonzalez, P., Pines, J., and Desai, A. (2021). Spindle assembly checkpoint activation and silencing at kinetochores. Semin Cell Dev Biol *117*, 86-98. 10.1016/j.semcdb.2021.06.009.
5. McAinsh, A.D., and Kops, G. (2023). Principles and dynamics of spindle assembly checkpoint signalling. Nature reviews *24*, 543-559. 10.1038/s41580-023-00593-z.
6. Vazquez-Novelle, M.D., Sansregret, L., Dick, A.E., Smith, C.A., McAinsh, A.D., Gerlich, D.W., and Petronczki, M. (2014). Cdk1 inactivation terminates mitotic checkpoint surveillance and stabilizes kinetochore attachments in anaphase. Curr Biol *24*, 638-645. 10.1016/j.cub.2014.01.034.
7. Rattani, A., Vinod, P.K., Godwin, J., Tachibana-Konwalski, K., Wolna, M., Malumbres, M., Novak, B., and Nasmyth, K. (2014). Dependency of the spindle assembly checkpoint on Cdk1 renders the anaphase transition irreversible. Curr Biol *24*, 630-637. 10.1016/j.cub.2014.01.033.
8. Collin, P., Nashchekina, O., Walker, R., and Pines, J. (2013). The spindle assembly checkpoint works like a rheostat rather than a toggle switch. Nature cell biology *15*, 1378-1385. 10.1038/ncb2855 ncb2855 [pii].
9. Dick, A.E., and Gerlich, D.W. (2013). Kinetic framework of spindle assembly checkpoint signalling. Nature cell biology *15*, 1370-1377. 10.1038/ncb2842 ncb2842 [pii].
10. Rosenberg, J.S., Cross, F.R., and Funabiki, H. (2011). KNL1/Spc105 recruits PP1 to silence the spindle assembly checkpoint. Curr Biol *21*, 942-947. 10.1016/j.cub.2011.04.011.
11. Moura, M., Osswald, M., Leca, N., Barbosa, J., Pereira, A.J., Maiato, H., Sunkel, C.E., and Conde, C. (2017). Protein Phosphatase 1 inactivates Mps1 to ensure efficient Spindle Assembly Checkpoint silencing. Elife *6*, e25366. 10.7554/eLife.25366.
12. Grallert, A., Boke, E., Hagting, A., Hodgson, B., Connolly, Y., Griffiths, J.R., Smith, D.L., Pines, J., and Hagan, I.M. (2015). A PP1-PP2A phosphatase relay controls mitotic progression. Nature *517*, 94-98. 10.1038/nature14019.
13. Hayward, D., Alfonso-Pérez, T., Cundell, M.J., Hopkins, M., Holder, J.,

Bancroft, J., Hutter, L.H., Novak, B., Barr, F.A., and Gruneberg, U. (2019). CDK1-CCNB1 creates a spindle checkpoint-permissive state by enabling MPS1 kinetochore localization. The Journal of cell biology *218*, 1182-1199. 10.1083/jcb.201808014.

14. Alfonso-Pérez, T., Hayward, D., Holder, J., Gruneberg, U., and Barr, F.A. (2019). MAD1-dependent recruitment of CDK1-CCNB1 to kinetochores promotes spindle checkpoint signaling. The Journal of cell biology *218*, 1108-1117. 10.1083/jcb.201808015.
15. Allan, L.A., Camacho Reis, M., Ciossani, G., Huis In 't Veld, P.J., Wohlgemuth, S., Kops, G.J., Musacchio, A., and Saurin, A.T. (2020). Cyclin B1 scaffolds MAD1 at the kinetochore corona to activate the mitotic checkpoint. The EMBO journal *39*, e103180. 10.15252/embj.2019103180.
16. Hiruma, Y., Sacristan, C., Pachis, S.T., Adamopoulos, A., Kuijt, T., Ubbink, M., von Castelmur, E., Perrakis, A., and Kops, G.J. (2015). CELL DIVISION CYCLE. Competition between MPS1 and microtubules at kinetochores regulates spindle checkpoint signaling. Science (New York, N.Y *348*, 1264-1267. 10.1126/science.aaa4055.
17. Ji, Z., Gao, H., and Yu, H. (2015). CELL DIVISION CYCLE. Kinetochore attachment sensed by competitive Mps1 and microtubule binding to Ndc80C. Science (New York, N.Y *348*, 1260-1264. 10.1126/science.aaa4029.
18. Howell, B.J., McEwen, B.F., Canman, J.C., Hoffman, D.B., Farrar, E.M., Rieder, C.L., and Salmon, E.D. (2001). Cytoplasmic dynein/dynactin drives kinetochore protein transport to the spindle poles and has a role in mitotic spindle checkpoint inactivation. The Journal of cell biology *155*, 1159-1172.
19. Wojcik, E., Basto, R., Serr, M., Scaerou, F., Karess, R., and Hays, T. (2001). Kinetochore dynein: its dynamics and role in the transport of the Rough deal checkpoint protein. Nature cell biology *3*, 1001-1007.
20. Gassmann, R., Holland, A.J., Varma, D., Wan, X., Civril, F., Cleveland, D.W., Oegema, K., Salmon, E.D., and Desai, A. (2010). Removal of Spindly from microtubule-attached kinetochores controls spindle checkpoint silencing in human cells. Genes & development *24*, 957-971. 10.1101/gad.1886810.
21. Ide, A.H., DeLuca, K.F., Wiggan, O., Markus, S.M., and DeLuca, J.G. (2023). The role of kinetochore dynein in checkpoint silencing is restricted to disassembly of the corona. Molecular biology of the cell *34*, ar76. 10.1091/mbc.E23-04-0130.
22. Barisic, M., Sohm, B., Mikolcevic, P., Wandke, C., Rauch, V., Ringer, T., Hess, M., Bonn, G., and Geley, S. (2010). Spindly/CCDC99 is required for efficient chromosome congression and mitotic checkpoint regulation. Molecular biology of the cell *21*, 1968-1981. 10.1091/mbc.e09-04-0356.
23. McEwen, B.F., Heagle, A.B., Cassels, G.O., Buttle, K.F., and Rieder, C.L. (1997). Kinetochore fiber maturation in PtK1 cells and its implications for the mechanisms of chromosome congression and anaphase onset. J. Cell Biol. *137*, 1567-1580. 10.1083/jcb.137.7.1567.

24. Nicklas, R.B., Waters, J.C., Salmon, E.D., and Ward, S.C. (2001). Checkpoint signals in grasshopper meiosis are sensitive to microtubule attachment, but tension is still essential. Journal of cell science *114*, 4173-4183. 10.1242/jcs.114.23.4173.
25. Kuhn, J., and Dumont, S. (2019). Mammalian kinetochores count attached microtubules in a sensitive and switch-like manner. The Journal of cell biology. 10.1083/jcb.201902105.
26. Etemad, B., Vertesy, A., Kuijt, T.E.F., Sacristan, C., van Oudenaarden, A., and Kops, G. (2019). Spindle checkpoint silencing at kinetochores with submaximal microtubule occupancy. Journal of cell science *132*. 10.1242/jcs.231589.
27. Dudka, D., Noatynska, A., Smith, C.A., Liaudet, N., McAinsh, A.D., and Meraldi, P. (2018). Complete microtubule-kinetochore occupancy favours the segregation of merotelic attachments. Nat Commun *9*, 2042. 10.1038/s41467-018-04427-x.
28. Pereira, A.J., and Maiato, H. (2012). Maturation of the kinetochore-microtubule interface and the meaning of metaphase. Chromosome Res *20*, 563-577. 10.1007/s10577-012-9298-8.
29. Meitinger, F., Belal, H., Davis, R.L., Martinez, M.B., Shiau, A.K., Oegema, K., and Desai, A. (2024). Control of cell proliferation by memories of mitosis. Science (New York, N.Y *383*, 1441-1448. 10.1126/science.add9528.
30. Sparr, C., and Meitinger, F. (2025). Prolonged mitosis: A key indicator for detecting stressed and damaged cells. Current opinion in cell biology *92*, 102449. 10.1016/j.ceb.2024.102449.
31. Meitinger, F., Anzola, J.V., Kaulich, M., Richardson, A., Stender, J.D., Benner, C., Glass, C.K., Dowdy, S.F., Desai, A., Shiau, A.K., and Oegema, K. (2016). 53BP1 and USP28 mediate p53 activation and G1 arrest after centrosome loss or extended mitotic duration. The Journal of cell biology *214*, 155-166. 10.1083/jcb.201604081.
32. Lambrus, B.G., Daggubati, V., Uetake, Y., Scott, P.M., Clutario, K.M., Sluder, G., and Holland, A.J. (2016). A USP28-53BP1-p53-p21 signaling axis arrests growth after centrosome loss or prolonged mitosis. The Journal of cell biology *214*, 143-153. 10.1083/jcb.201604054.
33. Fulcher, L.J., Batley, C., Sobajima, T., and Barr, F.A. (2025). Time as a danger signal promoting G1 arrest after mitosis. Trends in cell biology. 10.1016/j.tcb.2025.06.001.
34. Fong, C.S., Mazo, G., Das, T., Goodman, J., Kim, M., O'Rourke, B.P., Izquierdo, D., and Tsou, M.F. (2016). 53BP1 and USP28 mediate p53-dependent cell cycle arrest in response to centrosome loss and prolonged mitosis. Elife *5*. 10.7554/eLife.16270.
35. Uetake, Y., and Sluder, G. (2010). Prolonged prometaphase blocks daughter cell proliferation despite normal completion of mitosis. Curr Biol *20*, 1666-1671. 10.1016/j.cub.2010.08.018.
36. Uetake, Y., and Sluder, G. (2018). Activation of the apoptotic pathway during prolonged prometaphase blocks daughter cell proliferation. Molecular biology of the cell *29*, 2632-2643. 10.1091/mbc.E18-01-0026.

37. Brinkley, B.R., Valdivia, M.M., Tousson, A., and Brenner, S.L. (1984). Compound kinetochores of the Indian muntjac. Evolution by linear fusion of unit kinetochores. Chromosoma *91*, 1-11.
38. Chi, J.X., Huang, L., Nie, W., Wang, J., Su, B., and Yang, F. (2005). Defining the orientation of the tandem fusions that occurred during the evolution of Indian muntjac chromosomes by BAC mapping. Chromosoma *114*, 167-172. 10.1007/s00412-005-0004-x.
39. Wurster, D.H., and Benirschke, K. (1970). Indian muntjac, Muntiacus muntjak: a deer with a low diploid chromosome number. Science *168*, 1364-1366. 10.1126/science.168.3937.1364.
40. Comings, D.E., and Okada, T.A. (1971). Fine structure of kinetochore in Indian muntjac. Exp Cell Res *67*, 97-110.
41. Drpic, D., Almeida, A.C., Aguiar, P., Renda, F., Damas, J., Lewin, H.A., Larkin, D.M., Khodjakov, A., and Maiato, H. (2018). Chromosome Segregation Is Biased by Kinetochore Size. Curr Biol *28*, 1344-1356 e1345. 10.1016/j.cub.2018.03.023.
42. Almeida, A.C., Drpic, D., Okada, N., Bravo, J., Madureira, M., and Maiato, H. (2020). Functional Dissection of Mitosis Using Immortalized Fibroblasts from the Indian Muntjac, a Placental Mammal with Only Three Chromosomes. Methods Mol. Biol. *2101*, 247-266. 10.1007/978-1-0716-0219-5_16.
43. Almeida, A.C., Soares-de-Oliveira, J., Drpic, D., Cheeseman, L.P., Damas, J., Lewin, H.A., Larkin, D.M., Aguiar, P., Pereira, A.J., and Maiato, H. (2022). Augmin-dependent microtubule self-organization drives kinetochore fiber maturation in mammals. Cell Rep *39*, 110610. 10.1016/j.celrep.2022.110610.
44. Howell, B.J., Moree, B., Farrar, E.M., Stewart, S., Fang, G., and Salmon, E.D. (2004). Spindle checkpoint protein dynamics at kinetochores in living cells. Curr Biol *14*, 953-964. 10.1016/j.cub.2004.05.053
S0960982204003860 [pii].
45. Shah, J.V., Botvinick, E., Bonday, Z., Furnari, F., Berns, M., and Cleveland, D.W. (2004). Dynamics of centromere and kinetochore proteins; implications for checkpoint signaling and silencing. Curr Biol *14*, 942-952. 10.1016/j.cub.2004.05.046.
46. Kuhn, J., and Dumont, S. (2017). Spindle assembly checkpoint satisfaction occurs via end-on but not lateral attachments under tension. The Journal of cell biology *216*, 1533-1542. 10.1083/jcb.201611104.
47. Kapoor, T.M., Lampson, M.A., Hergert, P., Cameron, L., Cimini, D., Salmon, E.D., McEwen, B.F., and Khodjakov, A. (2006). Chromosomes can congress to the metaphase plate before biorientation. Science (New York, N.Y *311*, 388-391. 311/5759/388 [pii]
10.1126/science.1122142.
48. Barisic, M., Aguiar, P., Geley, S., and Maiato, H. (2014). Kinetochore motors drive congression of peripheral polar chromosomes by overcoming random arm-ejection forces. Nature cell biology *16*. 10.1038/ncb3060.
49. Itoh, G., Ikeda, M., Iemura, K., Amin, M.A., Kuriyama, S., Tanaka, M.,

Mizuno, N., Osakada, H., Haraguchi, T., and Tanaka, K. (2018). Lateral attachment of kinetochores to microtubules is enriched in prometaphase rosette and facilitates chromosome alignment and bi-orientation establishment. Scientific Reports *8*, 3888. 10.1038/s41598-018-22164-5.

50. Vukusic, K., and Tolic, I.M. (2025). CENP-E initiates chromosome congression by opposing Aurora kinases to promote end-on attachments. Nat Commun *16*, 8537. 10.1038/s41467-025-64148-w.

51. Kwiatkowski, N., Jelluma, N., Filippakopoulos, P., Soundararajan, M., Manak, M.S., Kwon, M., Choi, H.G., Sim, T., Deveraux, Q.L., Rottmann, S., et al. (2010). Small-molecule kinase inhibitors provide insight into Mps1 cell cycle function. Nat Chem Biol *6*, 359-368. 10.1038/nchembio.345
nchembio.345 [pii].

52. Vassilev, L.T., Tovar, C., Chen, S., Knezevic, D., Zhao, X., Sun, H., Heimbrook, D.C., and Chen, L. (2006). Selective small-molecule inhibitor reveals critical mitotic functions of human CDK1. Proceedings of the National Academy of Sciences of the United States of America *103*, 10660-10665. 10.1073/pnas.0600447103.

53. Peretti, D., Maraschio, P., Lambiase, S., Lo Curto, F., and Zuffardi, O. (1986). Indirect immunofluorescence of inactive centromeres as indicator of centromeric function. Human genetics *73*, 12-16.

54. Cherry, L.M., and Johnston, D.A. (1987). Size variation in kinetochores of human chromosomes. Human genetics *75*, 155-158.

55. Cherry, L.M., Faulkner, A.J., Grossberg, L.A., and Balczon, R. (1989). Kinetochore size variation in mammalian chromosomes: an image analysis study with evolutionary implications. Journal of cell science *92 (Pt 2)*, 281-289.

56. Sanchez, L., Martinez, P., and Goyanes, V. (1991). Analysis of centromere size in human chromosomes 1, 9, 15, and 16 by electron microscopy. Genome *34*, 710-713.

57. Tomkiel, J., Cooke, C.A., Saitoh, H., Bernat, R.L., and Earnshaw, W.C. (1994). CENP-C is required for maintaining proper kinetochore size and for a timely transition to anaphase. The Journal of cell biology *125*, 531-545.

58. Nixon, F.M., Honnor, T.R., Clarke, N.I., Starling, G.P., Beckett, A.J., Johansen, A.M., Brettschneider, J.A., Prior, I.A., and Royle, S.J. (2017). Microtubule organization within mitotic spindles revealed by serial block face scanning EM and image analysis. Journal of cell science. 10.1242/jcs.203877.

59. Logsdon, G.A., Rozanski, A.N., Ryabov, F., Potapova, T., Shepelev, V.A., Catacchio, C.R., Porubsky, D., Mao, Y., Yoo, D., Rautiainen, M., et al. (2024). The variation and evolution of complete human centromeres. Nature. 10.1038/s41586-024-07278-3.

60. Parl, F.F. (2024). Analysis of CENP-B Boxes as Anchor of Kinetochores in Centromeres of Human Chromosomes. Bioinform Biol Insights *18*, 11779322241248913. 10.1177/11779322241248913.

61. Kixmoeller, K., Tarasovetc, E.V., Mer, E., Chang, Y.W., and Black, B.E.

(2025). Centromeric chromatin clearings demarcate the site of kinetochore formation. Cell. 10.1016/j.cell.2024.12.025.

62. Pereira, A., Sousa, M., Almeida, A.C., Ferreira, L.T., Costa, A.R., Novais-Cruz, M., Ferras, C., Sousa, M.M., Sampaio, P., Belsley, M., and Maiato, H. (2019). Coherent-hybrid STED: high contrast sub-diffraction imaging using a bi-vortex depletion beam. Optics express *27*, 8092-8111. 10.1364/OE.27.008092.

63. Zaytsev, A.V., Sundin, L.J., DeLuca, K.F., Grishchuk, E.L., and DeLuca, J.G. (2014). Accurate phosphoregulation of kinetochore-microtubule affinity requires unconstrained molecular interactions. The Journal of cell biology *206*, 45-59. 10.1083/jcb.201312107 jcb.201312107 [pii].

64. Volkov, V.A., Huis In 't Veld, P.J., Dogterom, M., and Musacchio, A. (2018). Multivalency of NDC80 in the outer kinetochore is essential to track shortening microtubules and generate forces. Elife *7*. 10.7554/eLife.36764.

65. Stimac, V., Koprivec, I., Manenica, M., Simunic, J., and Tolic, I.M. (2022). Augmin prevents merotelic attachments by promoting proper arrangement of bridging and kinetochore fibers. Elife *11*. 10.7554/eLife.83287.

66. Thompson, S.L., and Compton, D.A. (2010). Proliferation of aneuploid human cells is limited by a p53-dependent mechanism. The Journal of cell biology *188*, 369-381. 10.1083/jcb.200905057.

67. Santaguida, S., Richardson, A., Iyer, D.R., M'Saad, O., Zasadil, L., Knouse, K.A., Wong, Y.L., Rhind, N., Desai, A., and Amon, A. (2017). Chromosome Mis-segregation Generates Cell-Cycle-Arrested Cells with Complex Karyotypes that Are Eliminated by the Immune System. Developmental cell *41*, 638-651 e635. 10.1016/j.devcel.2017.05.022.

68. Hinchcliffe, E.H., Day, C.A., Karanjeet, K.B., Fadness, S., Langfald, A., Vaughan, K.T., and Dong, Z. (2016). Chromosome missegregation during anaphase triggers p53 cell cycle arrest through histone H3.3 Ser31 phosphorylation. Nature cell biology *18*, 668-675. 10.1038/ncb3348.

69. Giam, M., Wong, C.K., Low, J.S., Sinelli, M., Dreesen, O., and Rancati, G. (2020). P53 induces senescence in the unstable progeny of aneuploid cells. Cell Cycle *19*, 3508-3520. 10.1080/15384101.2020.1850968.

70. Phan, T.P., Maryniak, A.L., Boatwright, C.A., Lee, J., Atkins, A., Tijhuis, A., Spierings, D.C., Bazzi, H., Foijer, F., Jordan, P.W., et al. (2021). Centrosome defects cause microcephaly by activating the 53BP1-USP28-TP53 mitotic surveillance pathway. The EMBO journal *40*, e106118. 10.15252/embj.2020106118.

71. Brito, D.A., and Rieder, C.L. (2006). Mitotic checkpoint slippage in humans occurs via cyclin B destruction in the presence of an active checkpoint. Curr Biol *16*, 1194-1200. 10.1016/j.cub.2006.04.043.

72. Gascoigne, K.E., and Taylor, S.S. (2008). Cancer cells display profound intra- and interline variation following prolonged exposure to antimitotic drugs. Cancer Cell *14*, 111-122. 10.1016/j.ccr.2008.07.002.

73. Renda, F., Magidson, V., Tikhonenko, I., Fisher, R., Miles, C., Mogilner, A., and Khodjakov, A. (2020). Effects of malleable kinetochore morphology on measurements of intrakinetochore tension. Open biology *10*, 200101. 10.1098/rsob.200101.
74. Sacristan, C., Samejima, K., Ruiz, L.A., Deb, M., Lambers, M.L.A., Buckle, A., Brackley, C.A., Robertson, D., Hori, T., Webb, S., et al. (2024). Vertebrate centromeres in mitosis are functionally bipartite structures stabilized by cohesin. Cell. 10.1016/j.cell.2024.04.014.
75. Altemose, N., Logsdon, G.A., Bzikadze, A.V., Sidhwani, P., Langley, S.A., Caldas, G.V., Hoyt, S.J., Uralsky, L., Ryabov, F.D., Shew, C.J., et al. (2022). Complete genomic and epigenetic maps of human centromeres. Science (New York, N.Y *376*, eabl4178. doi:10.1126/science.abl4178.
76. Zou, Y., Yi, X., Wright, W.E., and Shay, J.W. (2002). Human telomerase can immortalize Indian muntjac cells. Exp Cell Res *281*, 63-76.
77. Zhang, G., Kruse, T., Guasch Boldu, C., Garvanska, D.H., Coscia, F., Mann, M., Barisic, M., and Nilsson, J. (2019). Efficient mitotic checkpoint signaling depends on integrated activities of Bub1 and the RZZ complex. The EMBO journal *38*. 10.15252/embj.2018100977.
78. Lukinavicius, G., Reymond, L., D'Este, E., Masharina, A., Gottfert, F., Ta, H., Guther, A., Fournier, M., Rizzo, S., Waldmann, H., et al. (2014). Fluorogenic probes for live-cell imaging of the cytoskeleton. Nat Methods *11*, 731-733. 10.1038/nmeth.2972
nmeth.2972 [pii].
79. Schindelin, J., Arganda-Carreras, I., Frise, E., Kaynig, V., Longair, M., Pietzsch, T., Preibisch, S., Rueden, C., Saalfeld, S., Schmid, B., et al. (2012). Fiji: an open-source platform for biological-image analysis. Nat Methods *9*, 676-682. 10.1038/nmeth.2019.
80. Pereira, A.J., Matos, I., Lince-Faria, M., and Maiato, H. (2009). Dissecting mitosis with laser microsurgery and RNAi in Drosophila cells. Methods Mol Biol *545*, 145-164. 10.1007/978-1-60327-993-2_9.
81. Tinevez, J.Y., Perry, N., Schindelin, J., Hoopes, G.M., Reynolds, G.D., Laplantine, E., Bednarek, S.Y., Shorte, S.L., and Eliceiri, K.W. (2017). TrackMate: An open and extensible platform for single-particle tracking. Methods *115*, 80-90. 10.1016/j.ymeth.2016.09.016.
82. Kletter, T., Munoz, O., Reusch, S., Biswas, A., Halavatyi, A., Neumann, B., Kuropka, B., Zaburdaev, V., and Reber, S. (2025). Cell state-specific cytoplasmic density controls spindle architecture and scaling. Nature cell biology *27*, 959-971. 10.1038/s41556-025-01678-x.
83. Jeff Reback, W.M., jbrockmendel, Joris Van den Bossche, Tom Augspurger, Phillip Cloud, gfyoung, Sinhrks, Simon Hawkins, Adam Klein, Matthew Roeschke, Jeff Tratner, Terji Petersen, Chang She, William Ayd, MomIsBestFriend, Marc Garcia, Jeremy Schendel, Andy Hayden, … Martin Winkel (2020). pandas-dev/pandas: Pandas 1.1.3 (v1.1.3). Zenodo. .
84. VanderPlas, J., Granger, B., Heer, J., Moritz, D., Wongsuphasawat, K., Satyanarayan, A., Lees, E., Timofeev, I., Welsh, B., Sievert, S. (2018). Altair: Interactive Statistical Visualizations for Python. Journal of Open

Source Software *3*, 1057. https://doi.org/10.21105/joss.01057.

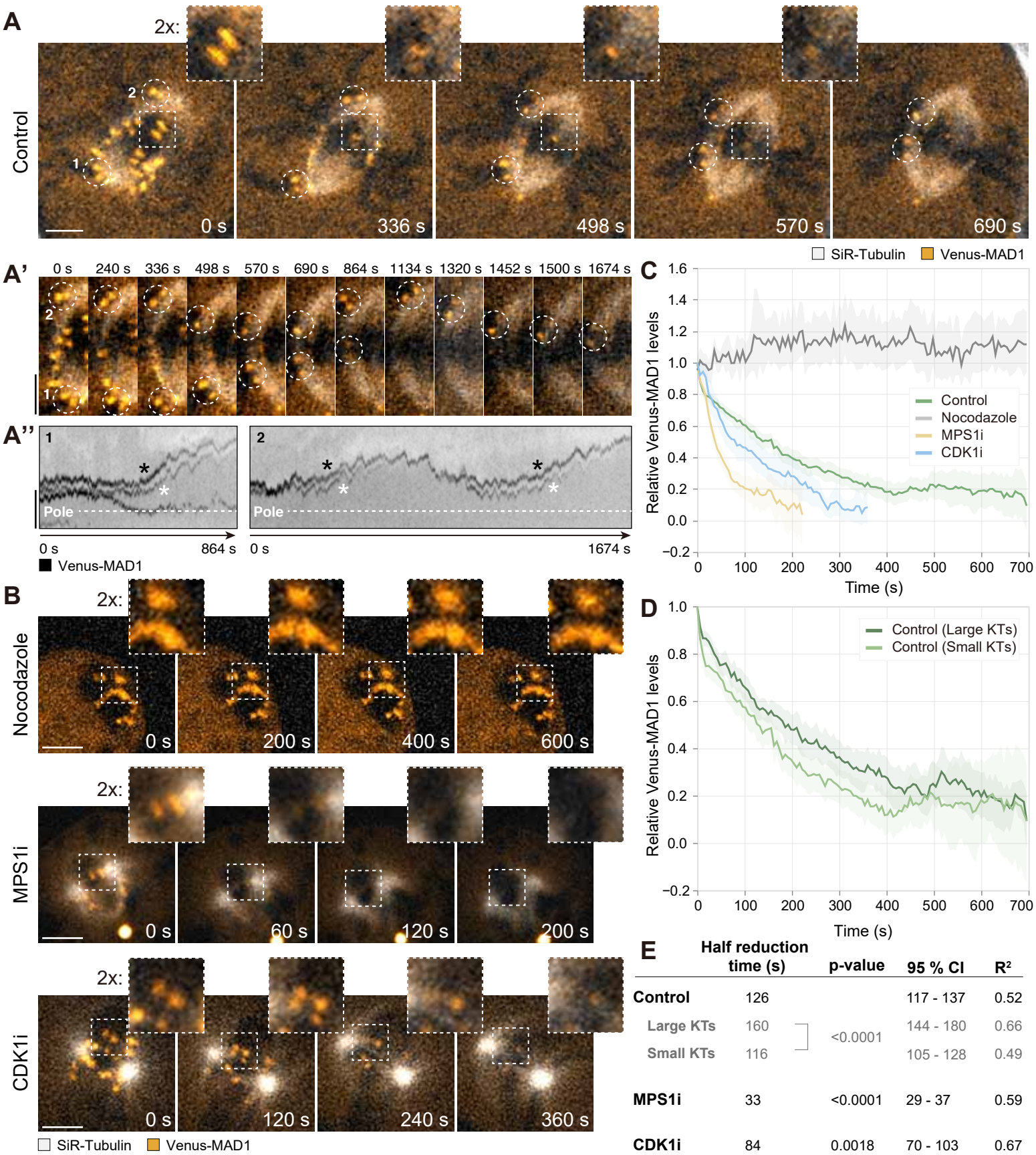

E

	Half reduction time (s)	p-value	95 % CI	R^2
Control	126		117 - 137	0.52
Large KTs	160	<0.0001	144 - 180	0.66
Small KTs	116		105 - 128	0.49
MPS1i	33	<0.0001	29 - 37	0.59
CDK1i	84	0.0018	70 - 103	0.67

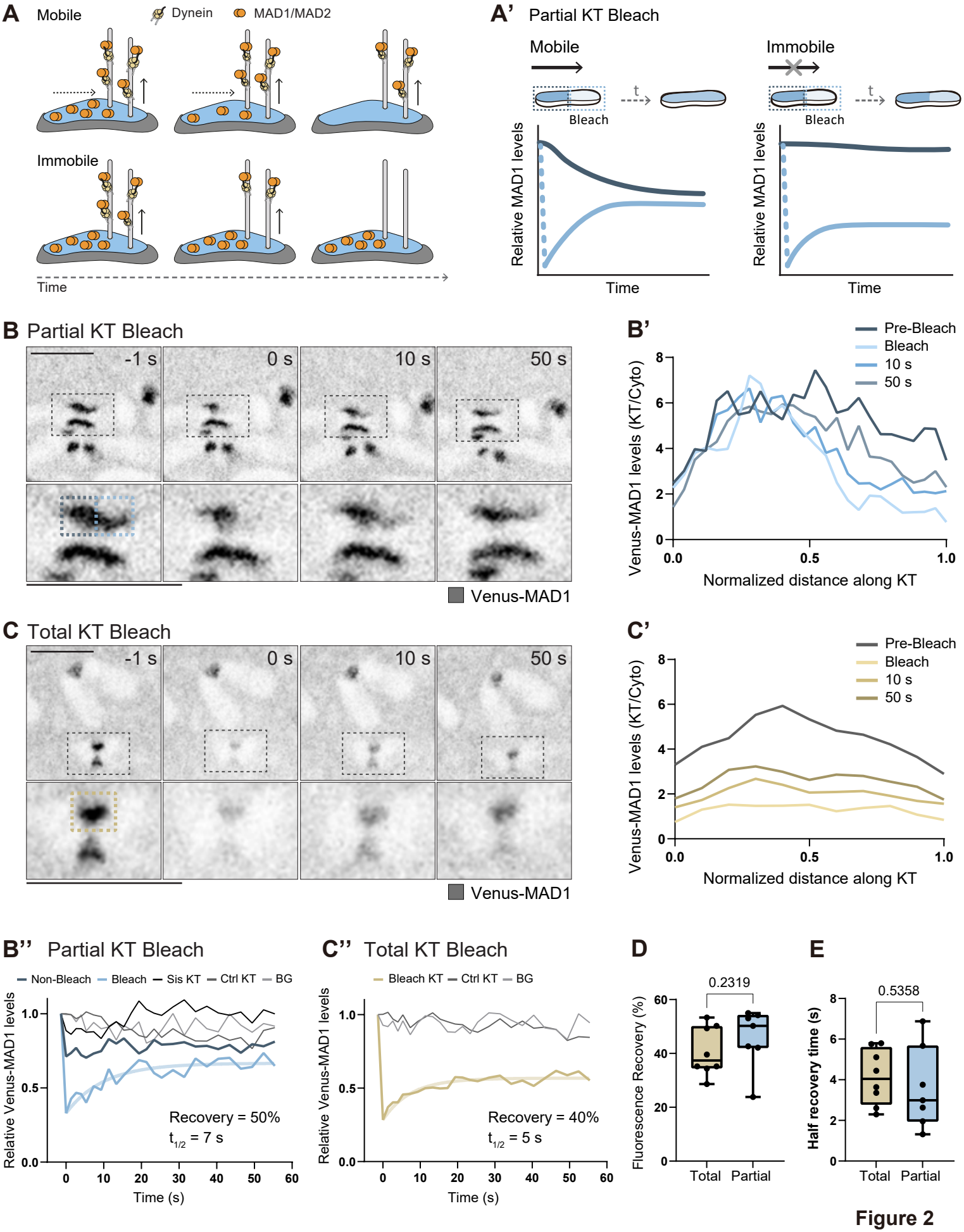
A
Mobile
Dynein
MAD1/MAD2
Immobile
Time
A'
Partial KT Bleach
Mobile
Immobile
Bleach
t
Relative MAD1 levels
Time
B
Partial KT Bleach
-1 s
0 s
10 s
50 s
Venus-MAD1
B'
Pre-Bleach
Bleach
10 s
50 s
Venus-MAD1 levels (KT/Cyto)
Normalized distance along KT
C
Total KT Bleach
C'
B''
Partial KT Bleach
Non-Bleach
Bleach
Sis KT
Ctrl KT
BG
Relative Venus-MAD1 levels
Recovery = 50%
$t_{1/2}$ = 7 s
Time (s)
C''
Total KT Bleach
Bleach KT
Ctrl KT
BG
Recovery = 40%
$t_{1/2}$ = 5 s
D
0.2319
Fluorescence Recovery (%)
Total
Partial
E
0.5358
Half recovery time (s)

Figure 2

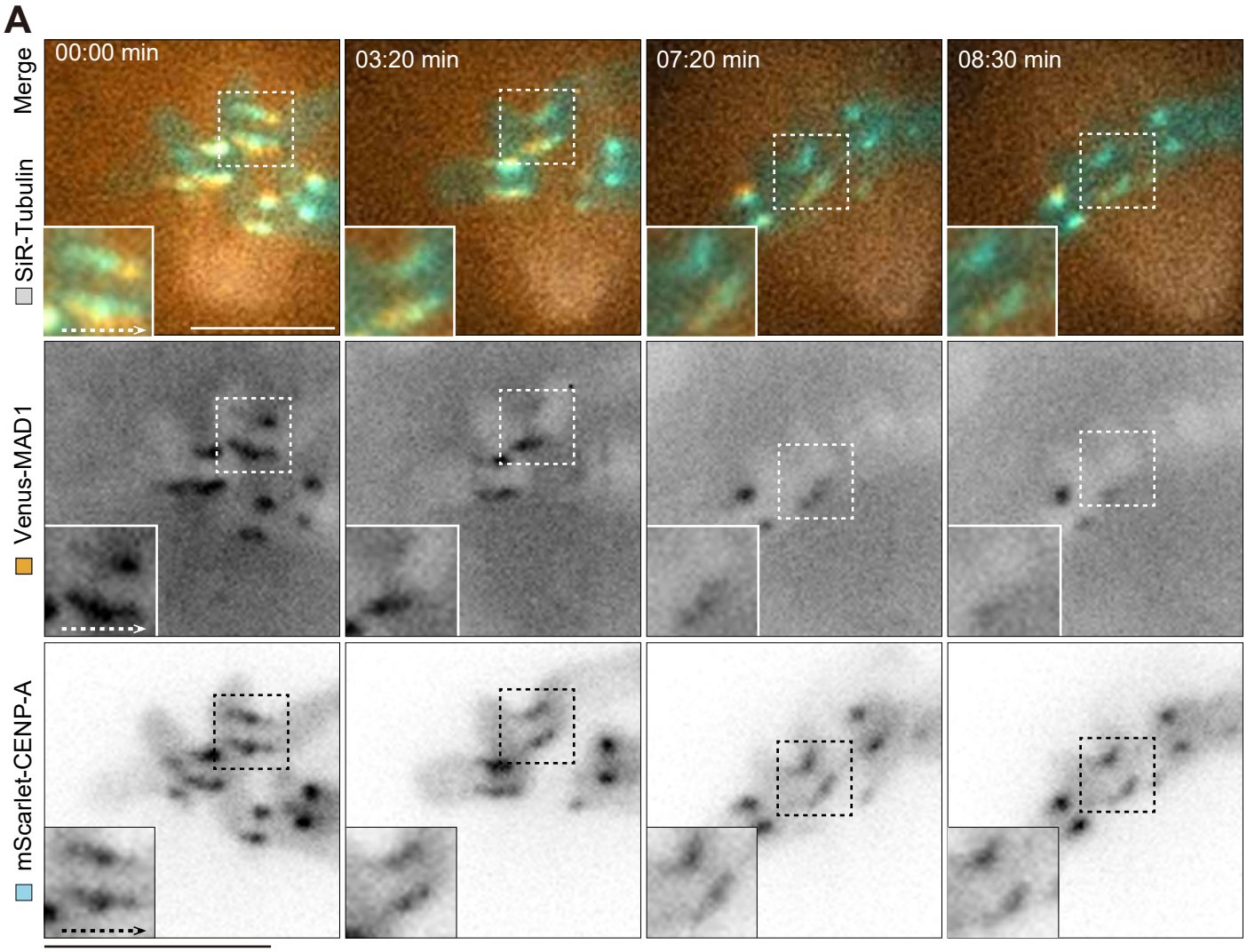
A
Merge
SiR-Tubulin
Venus-MAD1
mScarlet-CENP-A
00:00 min
03:20 min
07:20 min
08:30 min

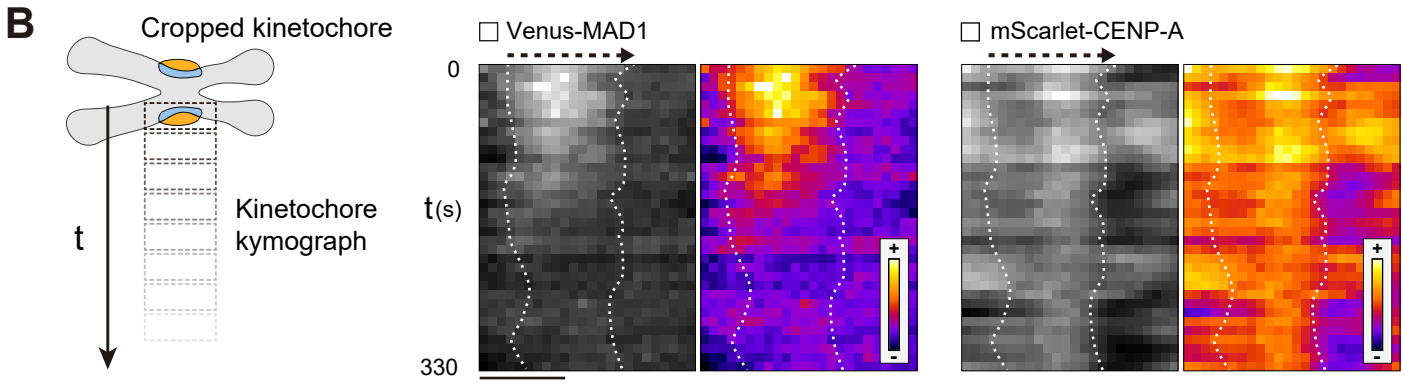
B
Cropped kinetochore
t
Kinetochore
kymograph
Venus-MAD1
mScarlet-CENP-A
0
t(s)
330
+
-

Figure 3

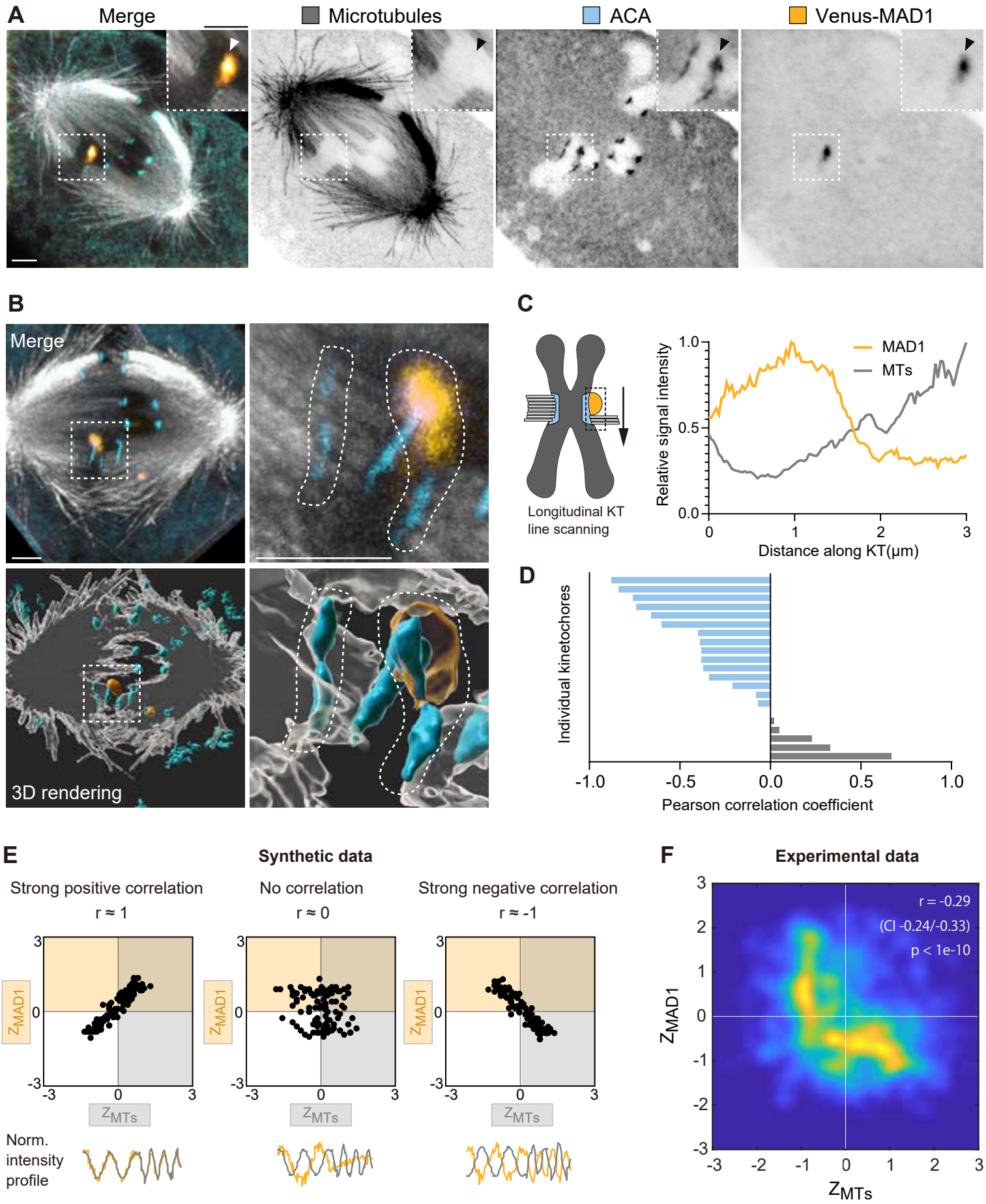
A
Merge
Microtubules
ACA
Venus-MAD1
B
Merge
3D rendering
C
Longitudinal KT line scanning
Relative signal intensity
MAD1
MTs
Distance along KT(µm)
D
Individual kinetochores
Pearson correlation coefficient
E
Synthetic data
Strong positive correlation
r ≈ 1
No correlation
r ≈ 0
Strong negative correlation
r ≈ -1
Z_MAD1
Z_MTs
Norm. intensity profile
F
Experimental data
r = -0.29
(CI -0.24/-0.33)
p < 1e-10
Z_MAD1
Z_MTs

Figure 4

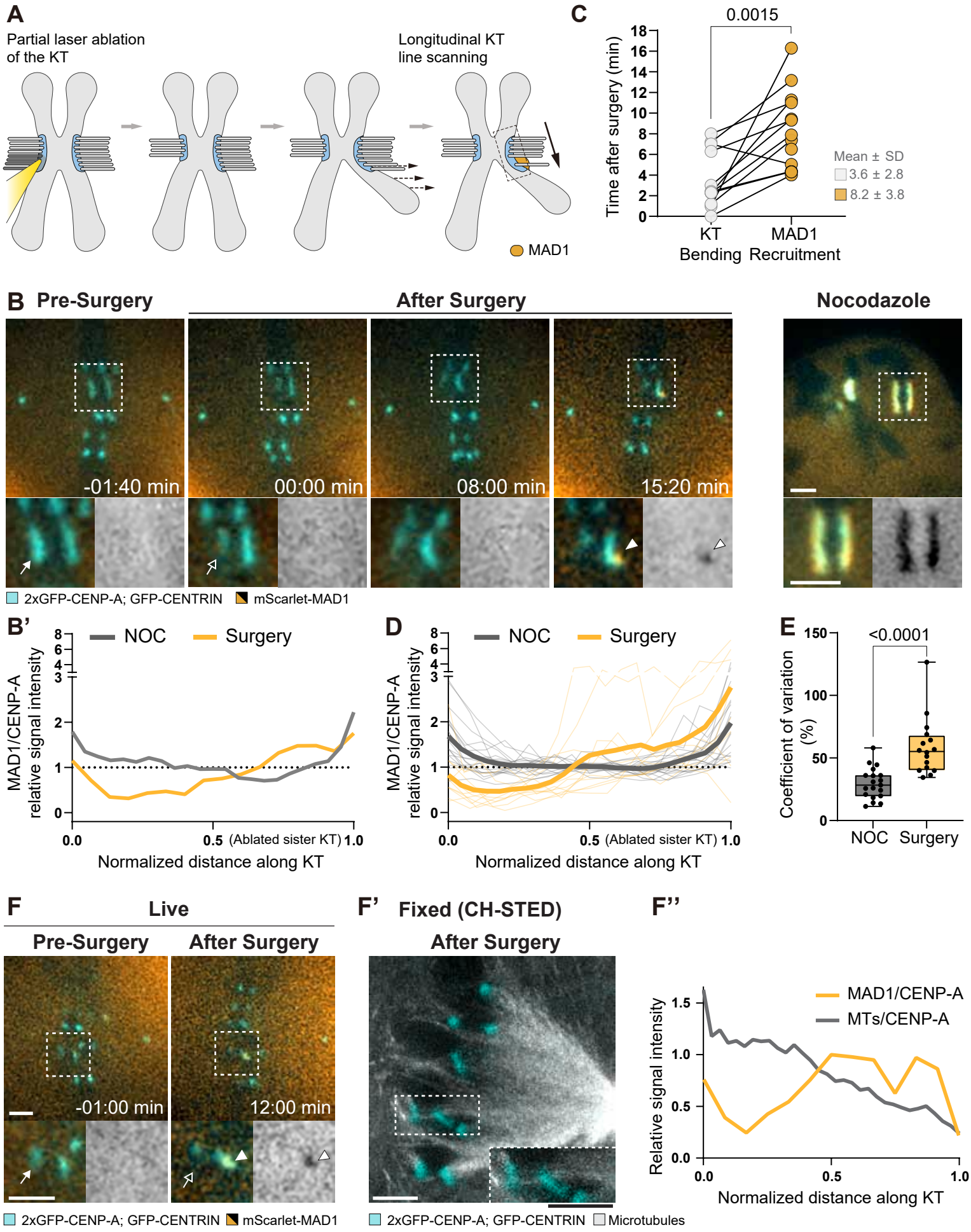
A
Partial laser ablation of the KT
Longitudinal KT line scanning
MAD1
C
0.0015
Time after surgery (min)
Mean ± SD
3.6 ± 2.8
8.2 ± 3.8
KT Bending
MAD1 Recruitment
B Pre-Surgery
After Surgery
Nocodazole
-01:40 min
00:00 min
08:00 min
15:20 min
2xGFP-CENP-A; GFP-CENTRIN
mScarlet-MAD1
B'
NOC
Surgery
MAD1/CENP-A relative signal intensity
(Ablated sister KT)
Normalized distance along KT
D
E
<0.0001
Coefficient of variation (%)
F Live
Pre-Surgery
After Surgery
-01:00 min
12:00 min
F' Fixed (CH-STED)
After Surgery
F''
MAD1/CENP-A
MTs/CENP-A
Relative signal intensity
Microtubules

Figure 5

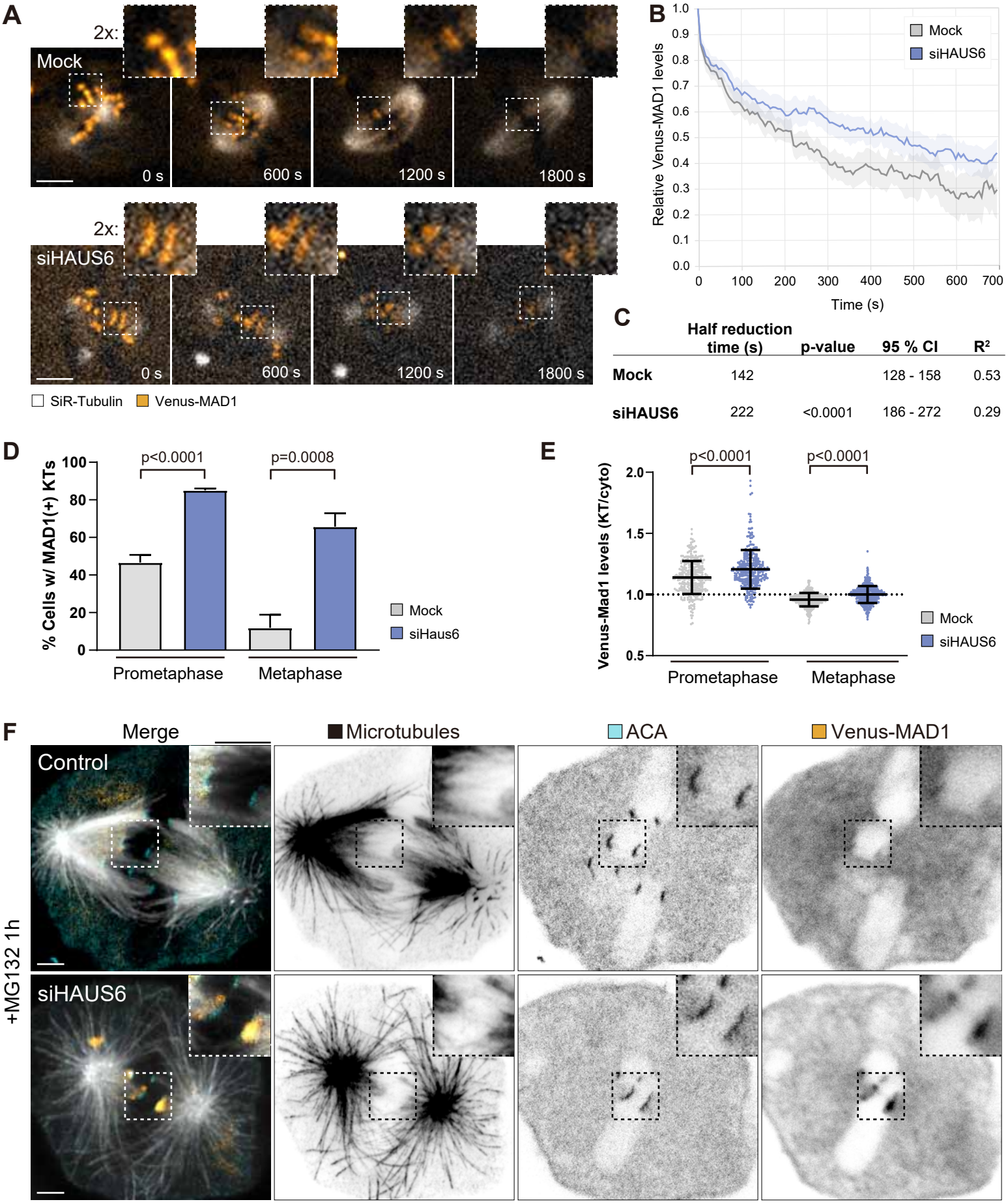

	Half reduction time (s)	p-value	95 % CI	R^2
Mock	142		128 - 158	0.53
siHAUS6	222	<0.0001	186 - 272	0.29

Figure 6

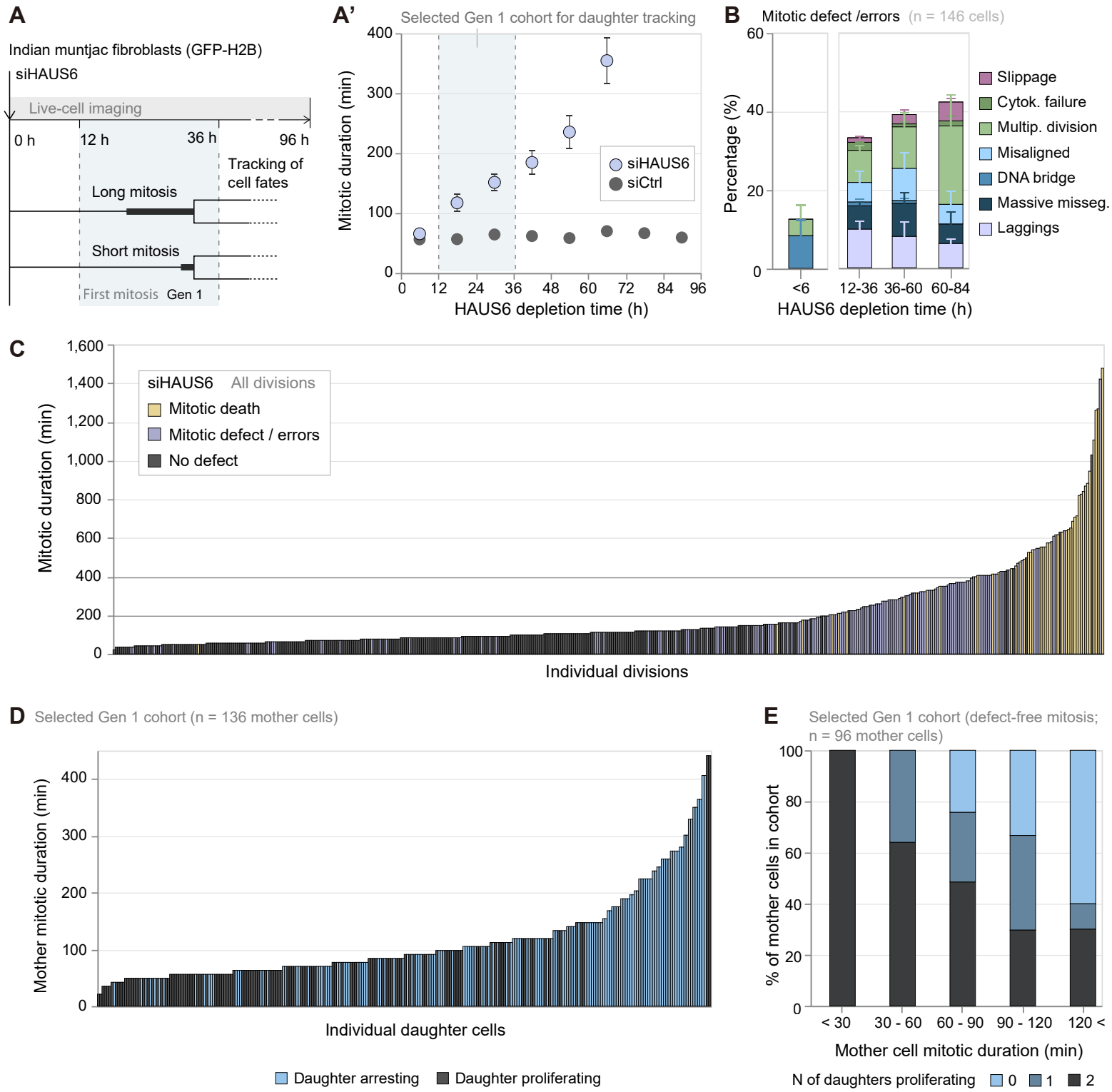
A
Indian muntjac fibroblasts (GFP-H2B)
siHAUS6
Live-cell imaging
0 h
12 h
36 h
96 h
Tracking of cell fates
Long mitosis
Short mitosis
First mitosis
Gen 1
A'
Selected Gen 1 cohort for daughter tracking
Mitotic duration (min)
HAUS6 depletion time (h)
siHAUS6
siCtrl
B
Mitotic defect /errors (n = 146 cells)
Percentage (%)
<6
12-36
36-60
60-84
HAUS6 depletion time (h)
Slippage
Cytok. failure
Multip. division
Misaligned
DNA bridge
Massive misseg.
Laggings
C
siHAUS6 All divisions
Mitotic death
Mitotic defect / errors
No defect
Mitotic duration (min)
Individual divisions
D
Selected Gen 1 cohort (n = 136 mother cells)
Mother mitotic duration (min)
Individual daughter cells
Daughter arresting
Daughter proliferating
E
Selected Gen 1 cohort (defect-free mitosis; n = 96 mother cells)
% of mother cells in cohort
< 30
30 - 60
60 - 90
90 - 120
120 <
Mother cell mitotic duration (min)
N of daughters proliferating
0
1
2

Figure 7

Augmin-mediated K-fiber maturation

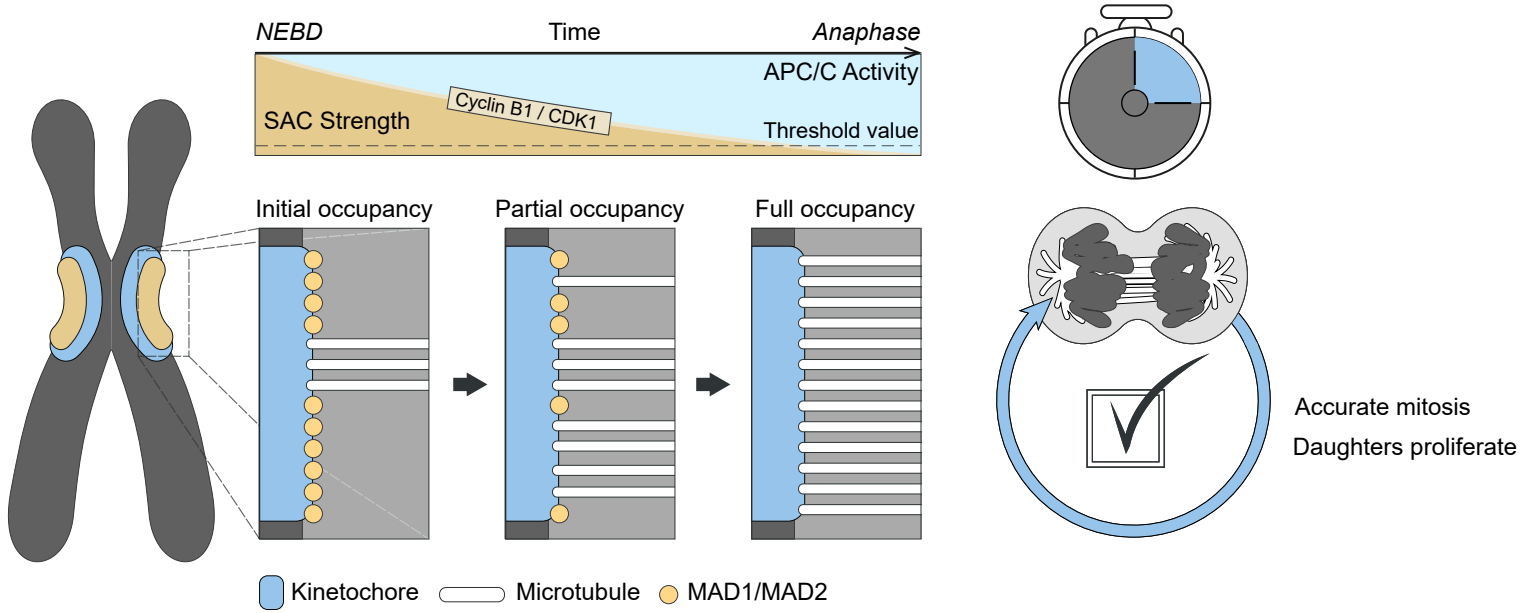
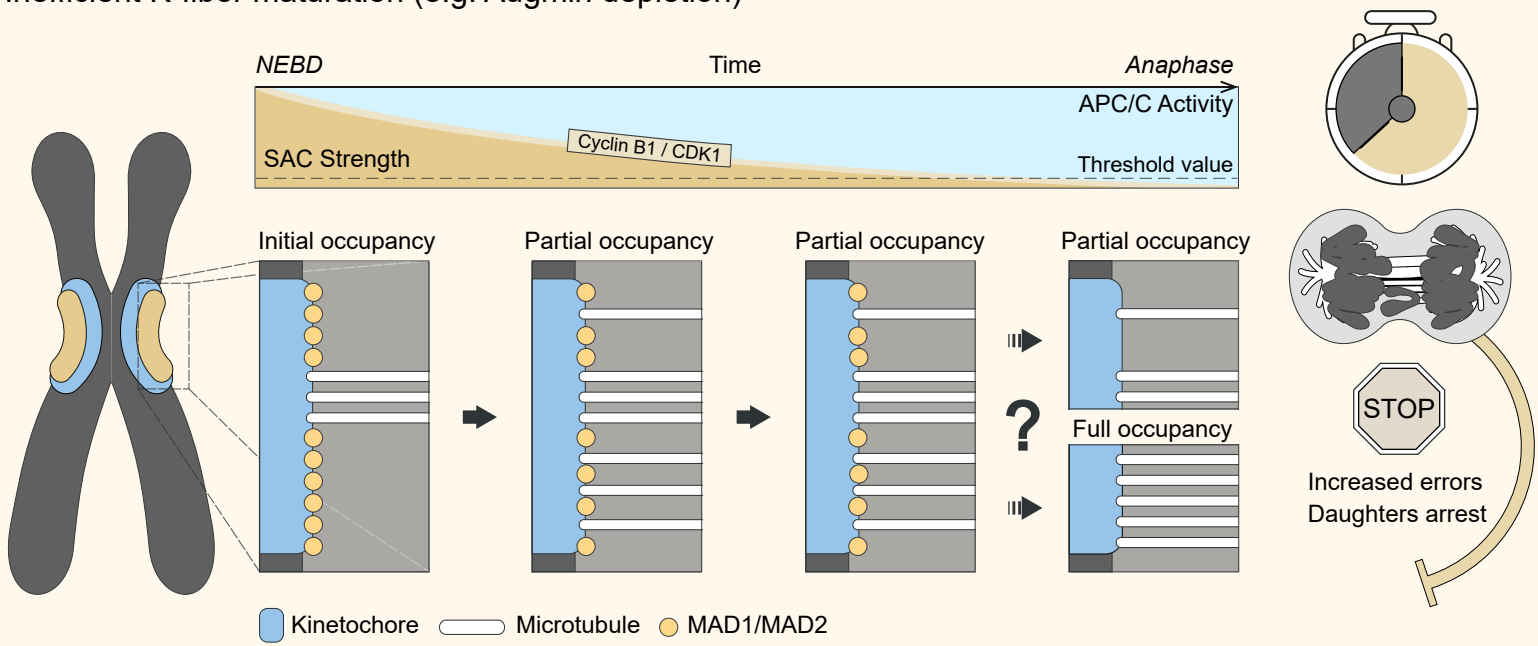
Inefficient K-fiber maturation (e.g. Augmin depletion)